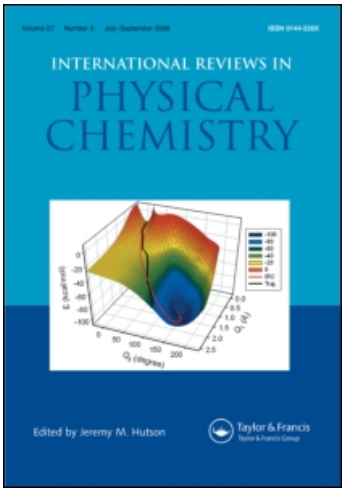

International Reviews in Physical Chemistry
Publication details, including instructions for authors and subscription information:
http://www.informaworld.com/smpp/title~content=t713724383

Photodissociation of simple aromatic molecules in a molecular beam

Chi-Kung Ni[a]; Yuan T. Lee[ab]
[a] Institute of Atomic and Molecular Sciences, Academia Sinica, Taipei, Taiwan [b] Department of Chemistry, National Taiwan University, Taipei 106, Taiwan

To cite this Article Ni, Chi-Kung and Lee, Yuan T.(2004) 'Photodissociation of simple aromatic molecules in a molecular beam', International Reviews in Physical Chemistry, 23: 2, 187 — 218
To link to this Article: DOI: 10.1080/01442350410001703799
URL: http://dx.doi.org/10.1080/01442350410001703799

INT. REVIEWS IN PHYSICAL CHEMISTRY, 2004
VOL. 23, NO. 2, 187–218

Taylor & Francis
Taylor & Francis Group

Photodissociation of simple aromatic molecules in a molecular beam

CHI-KUNG NI†* and YUAN T. LEE†‡
† Institute of Atomic and Molecular Sciences, Academia Sinica,
PO Box 23-166, Taipei, Taiwan
‡ Department of Chemistry, National Taiwan University,
Taipei 106, Taiwan

An overview is presented of our recent experimental studies of aromatic molecules using multimass ion imaging techniques. Photodissociation of benzene, fluorobenzene, toluene, *m*-xylene, ethylbenzene, propylbenzene and chlorotoluene at 248 nm or 193 nm was investigated under collisionless conditions. The photofragment translational energy distribution and dissociation rate of each dissociation channel were recorded. New isomerization and dissociation channels were observed from these studies. The data are discussed with reference to the *ab initio* potential energy surface and statistical theory results.

Contents

1. Introduction

Aromatic photochemistry has been a major area of study for several decades. The conspicuous feature that has emerged from studies in aromatic photochemistry is that the photoexcitation of aromatic molecules leads to a rich variety of reactions. Simple aromatic molecules show many regions of absorption. One of the common

* Author to whom correspondence should be addressed.
E-mail: ckni@po.iams.sinica.edu.tw

International Reviews in Physical Chemistry ISSN 0144–235X print/ISSN 1366–591X online
http://www.tandf.co.uk/journals
DOI: 10.1080/01442350410001703799

properties of aromatic molecules is that the excitation of the electrons of the phenyl ring corresponds to absorption in the UV region. Although additional absorption corresponding to the excitation of electrons of functional groups attached to the phenyl ring may occur in the same region, the photochemical properties of these two types of excitation can be very different. Excitation of the phenyl ring results in an excited state that is stable with respect to dissociation. For most of the benzene derivatives, the UV fluorescence quantum yields corresponding to the excitation of the phenyl ring decrease rapidly with an increase in photon energy [1–6]. Internal conversion, intersystem crossing and isomerization become important monomolecular processes in these molecules. For example, broad features appear in the high-energy levels of S_1–S_0 fluorescence spectra of alkylbenzenes [7], indicating 'rapid and irreversible' relaxation of these energy levels in the S_1 state. In addition, if the photon energy is larger than the bond energy, dissociation channels may open. Dissociation from this type of excitation must occur indirectly either through coupling of the stable and repulsive states or after internal conversion from an initial excited state to a lower electronic state. However, the properties of the excited states corresponding to the excitation of the functional groups attached to the phenyl ring depend strongly on the characteristics of the functional groups. Dissociation mechanisms related to these kinds of excitation could be very different from that of the phenyl ring.

As the photon energy increases to the higher electronic excited states of the phenyl ring, the internal conversion rates for most of the benzene derivatives increase rapidly, and the quantum yields of fluorescence and intersystem crossing become very small. As a result, most of the molecules after absorption of UV photons become highly vibrationally excited molecules, 'hot molecules', through internal conversion. However, the dissociation of a hot aromatic molecule is a fairly slow process because of the sharing of internal energy between a large number of vibrational degrees of freedom in the molecule. One of the very interesting aspects of benzene and its derivatives is that below the bond dissociation energy, there are many structural isomers, and the activation energy for isomerization also lies below the bond dissociation energy. Consequently, isomerization processes are expected to take place before a molecule finds its way to dissociate. Under collisionless conditions, energy in the molecules is conserved (except when deactivated by photon emission) and the molecules would not be deactivated and stabilized through isomerization. If the initial photon energy is larger than the dissociation threshold and no photon emission occurs, the molecules eventually dissociate into fragments. However, the dissociation rate and dissociation channels after isomerization can be very different from those of the molecules before isomerization.

The study these aromatic molecules is not straightforward because of the complicated photon energy dependence of the isomerization and dissociation channels as well as many possible sequential secondary reactions. However, these problems can be overcome by studying the photodissociation in a molecular beam (that is under collisionless conditions). As the molecules are not deactivated in collision-free conditions, dissociation and isomerization can be studied with a fixed internal energy. In addition, primary photofragments can be clearly identified without interference from secondary reactions. Furthermore, detailed molecular photodissociation mechanisms can be understood from measurements of the dissociation rates, fragment translational energy distributions, state distributions, and fragment angular distribution. In contrast to the collisionless conditions in a molecular beam, the dissociation mechanism and the primary dissociation fragments

are not easily determined in the condensed phase or in the high-pressure gas phase because of the collisions and consequent reactions.

Molecular photodissociation has been studied in a molecular beam by various experimental techniques. For state-specific detection, laser-induced fluorescence, multiphoton ionization and coherent laser scattering have provided extremely detailed information on the dynamics of photodissociation. Unfortunately, a large number of interesting polyatomic photofragments produced from aromatic molecules cannot be detected by these techniques because of the complexities of the spectra. The main advantage of photofragment translational spectroscopy using the ionization detection method is that it is universally applicable to all products. However, only a single mass at a given angle can be detected each time in the traditional translational spectroscopy measurement. This makes the measurement time-consuming for large molecules with many dissociation channels in the photodissociation process. We have constructed a new type of molecular beam apparatus [8, 9] in which the identification of dissociation products from many different channels and measurements of their translational energies can be carried out simultaneously. In addition, the high detection sensitivity allows us to study the photodissociation at very low photolysis laser fluence. Thus dissociation due to multiphoton absorption is eliminated. We have used this method to study the photodissociation of many aromatic molecules [10–20]. New dissociation channels and isomerization pathways were observed in these studies. In this review, the photodissociation dynamics of some simple aromatic molecules investigated using this new method are discussed.

2. Experimental methods

2.1. *Photofragment identification and translational energy measurement*

The experimental techniques have been described in detail in our previous reports [8, 9] and only a brief description is given here. The apparatus consisted of a molecular beam, a UV photolysis laser beam, an ionization VUV probe laser beam, a mass spectrometer, and a two-dimensional ion detector. A schematic diagram of the multimass ion imaging detection system is shown in figure 1.

Molecules in the molecular beam were photodissociated by a photolysis laser pulse. The recoil velocity of dissociation products and centre-of-mass velocity (molecular beam velocity) caused the fragments to expand into a large sphere on their flight to the ionization region, and they were then ionized by a VUV laser pulse. The distance and time delay between the VUV laser pulse and the photolysis laser pulse were set such that the time delay matched the velocity of the molecular beam. This time delay ensured that the VUV laser beam passed through the centre-of-mass of the dissociation products, and generated a line segment of photofragment ions by photoionization. There could be many fragment ions of different masses within this segment according to the photodissociation mechanisms of the parent molecules. Each fragment has its own intensity distribution along the segment. The length of the segment was proportional to the fragment recoil velocity in the centre-of-mass frame multiplied by the delay time.

After the VUV laser pulse had generated the ions, a pulsed electric field was used to extract the ions into a mass spectrometer to separate different masses within the ion segment. During the flight through the mass spectrometer, the length of the fragment ion segment kept expanding according to the fragment recoil velocity.

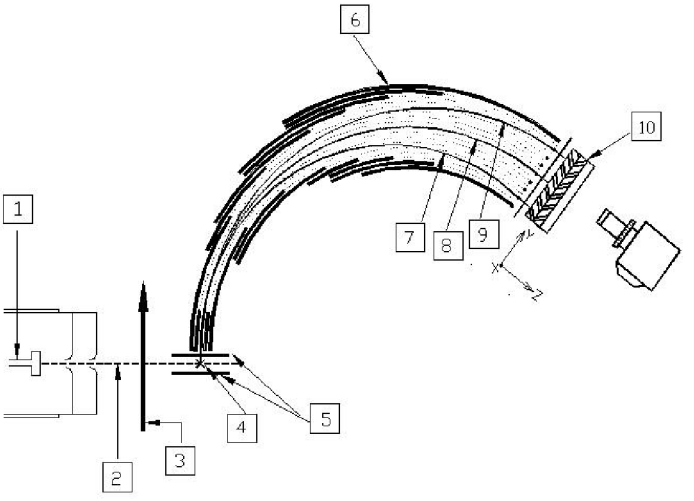

Figure 1. Schematic diagram of the multimass ion imaging detection system: (1) nozzle; (2) molecular beam; (3) photolysis laser beam; (4) VUV laser beam, which is perpendicular to the plane of the paper; (5) ion extraction plates; (6) energy analyser; (7–9) simulation ion trajectories of $m/e = 16$, 14, 12; (10) two-dimensional detector, where the Y-axis is the mass axis and the X-axis (perpendicular to the plane of the paper) is the velocity axis.

Meanwhile, ions of different masses started to separate from each other in the mass spectrometer. The trajectories of the different masses are illustrated in figure 1. Charge particles of smaller m/e values had larger radii in their trajectories and reached the upper part of the exit port. At the exit port of the energy analyser, a two-dimensional ion detector was used to detect the ion position and intensity distribution. In this two-dimensional detector, one direction was the recoil velocity axis (X-axis, as shown in figure 1) and the other was the mass axis (Y-axis, as shown in figure 1). The translational energy distributions in the centre-of-mass frame of many different fragments were obtained simultaneously from the position and intensity distributions of the image.

The change in the delay time between these two laser pulses had to match the distance between the crossing points of the photolysis laser beam and the VUV laser beam with the molecular beam, according to the velocity of the molecular beam, to ensure that the ionization laser passed through the centre-of-mass of the products. This adjustment also changed the length of the fragment ion segment in the image. The relation between the length of the ion image and the change in photolysis laser position (or delay time) is shown in figure 2. In general, the distance between these two crossing points was set to be long for the detection of fragments with small recoil velocity, and short for the detection of fragments with large recoil velocity.

If the dissociation rate was small, then some of molecules did not dissociate immediately after the absorption of the photolysis photons. Those molecules with large internal energy stayed within the molecular beam. They flew with almost the same velocity to the ionization region and were then ionized by the VUV laser, resulting in dissociative ionization (reaction 4). The ion image from dissociative

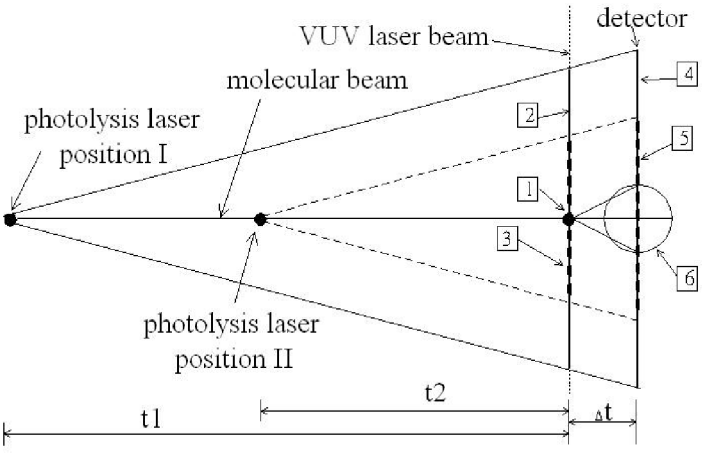

Figure 2. Relationship between the lengths of the images that result from different crossing points of the photolysis laser beam with the molecular beam. The disc-like image from the dissociation after ionization is also shown. (1) represents the crossing point of the molecular beam and the VUV laser beam, where the dissociative ionization (reaction 4) occurs. The disc-like image, represented by (6), is from these dissociative ionizations. (2) and (3) represent the lengths of fragment ion distribution created by the VUV laser photoionization from the photolysis laser at positions I and II, respectively. The line-shape images, represented by (4) and (5), are from these fragment ion distributions. t_1 and t_2 represent two different delay times between the photolysis laser pulse and the VUV laser pulse according to two different photolysis laser positions. Δt is the flight time of the fragment ion in the mass spectrometer.

ionization is very different from the image due to the dissociation products of neutral molecules (reactions 2 and 3).

$$A + h\nu_{UV} \rightarrow A^* \qquad \text{(excitation)} \qquad (1)$$

$$A^* \rightarrow B + C \qquad \text{(dissociation)} \qquad (2)$$

$$B + h\nu_{VUV} \rightarrow B^+ + e^-;\ C + h\nu_{VUV} \rightarrow C^+ + e^- \qquad \text{(fragment ionization)} \qquad (3)$$

$$A^* + h\nu_{VUV} \rightarrow D^+ + E + e^- \qquad \text{(dissociative ionization)} \qquad (4)$$

As the dissociation and ionization occurred at the same position, the image from the dissociative ionization is a 2D projection of the photofragment ion's 3D-recoil velocity distribution. It is a disc-like image and is different from the line-shape image resulting from dissociation products of neutral molecules. With the VUV laser fixed in position, only the intensity of the disc-like image changed with the delay time between two laser pulses, and the size of the disc-like image does not change with the delay time. Therefore, the ion image resulting from dissociative ionization can be distinguished easily from the image resulting from the dissociation products of neutral molecules by the shape of the image as well as by the change with the delay time.

2.2. *Dissociation rate measurement*

There are several methods to determine the dissociation rate, depending on the values of the rate. Dissociation rates can be obtained from the product growth with

respect to the delay time between the pump and probe laser pulses using a TOF mass spectrometer. An accurate measurement can be obtained only if the dissociation rate is large enough that most of the molecules dissociate into fragments before both molecular beam and fragments fly out of the detection region. Another method is to measure the rate of disappearance of the excited parent molecules [21]. For fast dissociation rates, this can be performed directly by measuring the decay of the products from dissociative ionization (reaction 4). For some molecules, the m/e value of the ion from dissociative ionization is the same as that from dissociation (reactions 2 and 3). The measurement is therefore the combination of product growth and parent decay. However, accurate dissociation rates can still be obtained as long as the dissociation rate is fast enough so that most of the excited parent molecules and fragments do not fly out of the probe region. However, when the dissociation rate is slow and the methods described above cannot be applied, the dissociation rate can be obtained from intensity changes of the disc-like images at various delay times (therefore, at various photolysis laser positions) along the molecular beam [10].

In addition to these methods, the dissociation rate can be obtained from the line-shape image intensity distribution. As the intensity of the line-shape image results from the accumulation of the products produced during the time period from the pump pulse to the probe pulse, the ion image intensity distribution is a function of both the fragment recoil velocity distribution and the dissociation rate. Therefore, both the velocity distribution and the dissociation rate can be obtained from the image. In our instrument, the image intensity profiles are sensitive to the dissociation rates when they are in the region between 10^4 and $10^6\,s^{-1}$. If the fragment image contains more than one component (either the disc-like images or multicomponents in the line-shape image), the dissociation rates and velocity distributions of each component can be determined separately from the forward convolution simulation of the images. This avoids fitting the experimental data obtained from the product growth or the parent decay to the multiexponential functions in a low signal-to-noise ratio situation.

In the work described below, the dissociation rates were obtained from the product growth with respect to the delay time if the dissociation rate was fast enough before the parent molecules and fragments flew out of the probe region. This is demonstrated in the photodissociation study of toluene, ethylbenzene and propylbenzene at 193 nm. Alternatively, dissociation rates were obtained from the disc-like image intensity decay for slow dissociation rates, as illustrated in the rate measurement of benzene. For multicomponent velocity dissociation channels, as in the dissociation of ethylbenzene and propylbenzene at 248 nm, the dissociation rate of each component was determined separately by forward convolution simulation of the images.

3. Photodissociation of simple aromatic molecules

3.1. *Benzene*

The photophysics and photochemistry processes of benzene have been studied extensively in the past few decades. Benzene is frequently used as an example for both theoretical and experimental investigations. The fluorescence quantum yield of benzene in the S_1 state decreases rapidly when the excitation wavelength is shorter than 244.5 nm, and this is interpreted as the result of a non-radiative pathway, called

channel three, by which vibrational energy in excess of about $3000\,cm^{-1}$ is lost at an anomalously rapid rate. The decay rate of benzene after excitation to the S_1 state has been measured below and above the channel-three threshold of 244.5 nm under collision-free conditions. As a result of these experiments [1–3], it can be concluded that the lifetimes are in nanosecond and picosecond regions, corresponding to the decay of the singlet S_1 below and above the channel-three threshold, respectively. The triplet state produced by intersystem crossing from S_1 has a longer lifetime, in the region of several hundred nanoseconds [4].

The energy required for the excitation to the S_2 state is much larger than some of the bond energies in benzene. Dissociation is thus likely to occur after the excitation to the S_2 state. Although there have been many studies on benzene after excitation to the S_2 state, the photodissociation processes of benzene are still not clear. In the photolysis of benzene at 184.9 nm [22, 23], the quantum yield for the disappearance of benzene was found to decrease from unity at the low pressure limit with increasing benzene or N_2 buffer gas pressure. From the pressure dependence of the quantum yields for the disappearance of benzene and the production of benzene isomers, a reaction mechanism proceeding through the vibrationally excited ground electronic state of benzene, 'hot benzene', was proposed [23, 24]. Hot benzene was produced through internal conversion from the electronically excited singlet state ($^1E_{1u}$ or $^1B_{1u}$) populated by 184.9 nm absorption. It has also been observed after 193 nm excitation to the $^1B_{1u}$ state [25].

The decay of benzene from the S_2 state under collision-free conditions has also been studied. Reilly and Kompa studied the nanosecond UV laser-induced multiphoton ionization/fragmentation processes. A rate equation model was used for the simulation and the lifetime of the S_2 state was estimated to be 20 ps [26]. The lifetime of the S_2 state of benzene has been determined directly by pump and probe measurement with 160 fs laser pulses [27]. Benzene in the S_2 state, produced by 200 nm excitation, was found to have fast internal conversion to the S_0 and S_1 states with a lifetime of approximately 40 fs; the decay of highly vibrationally excited S_1 states produced from this internal conversion occurred within 5–10 ps.

The main photoproducts of benzene vapour at 184.9 nm were reported to be an isomer of benzene [22, 23], subsequently identified as fulvene [28, 29], and polymers. Both *cis*- and *trans*-1,3-hexadien-5-yne [24, 30] and small amounts of methane, ethane, ethylene, hydrogen and acetylene were also observed [22, 31]. The other two isomers, benzvalene and Dewar benzene, were obtained only in the condensed phase, and the results were interpreted as being due to the formation of benzvalene and Dewar benzene with excess energy that must be rapidly dissipated if they were to survive [32, 33]. The photoproducts of methane, ethane, ethylene and acetylene indicate the existence of a ring-opening photodissociation processes. Photodissociation of benzene at 193 and 248 nm has been investigated in a molecular beam [34]. The H atom elimination, H_2 elimination and a ring-opening dissociation channel $C_6H_6 \rightarrow C_5H_3 + CH_3$ were observed. However, *ab initio* calculation [35] showed that the dissociation barrier of the ring-opening dissociation channel is very close to the 193 nm photon energy, and the branching ratio of the ring-opening channel is expected to be negligible.

We have used multimass ion imaging techniques to study the photodissociation of benzene at 248 and 193 nm [10, 12]. Figure 3 (*a*) shows the ion images of $m/e = 85$–80 obtained from the photodissociation of d_6-benzene at 193 nm. The images of $m/e = 85$ and 84 corresponded to the parent ions and the ^{13}C of the parent

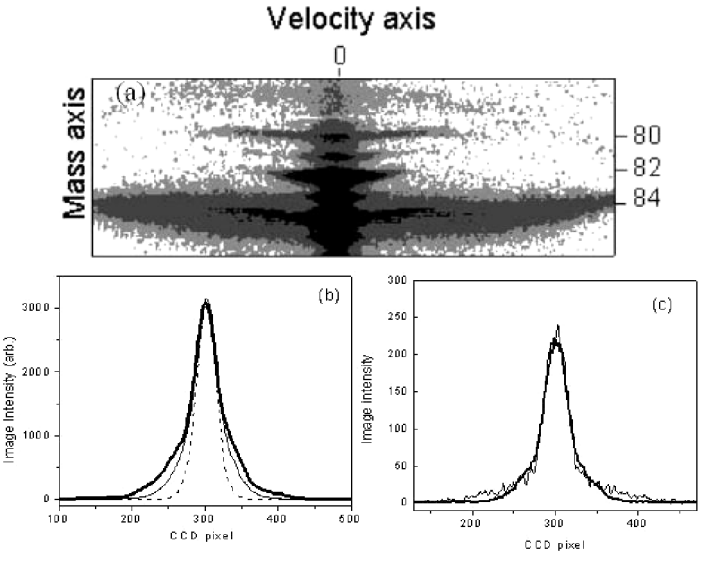

Figure 3. (*a*) The image of $m/e = 85$–80 from C_6D_6. (*b*) The image intensity profiles of $m/e = 80$ at delay times 124 μs (thick solid line), 94 μs (thin solid line) and 43 μs (dashed line). (*c*) The image intensity profiles of $m/e = 82$ at delay time 19 μs (thick solid line) and 43 μs (thin solid line).

ions, respectively. The images of $m/e = 83$ and 81 corresponded to 3% of the impurity C_6D_5H and the fragment of D elimination from the impurity, respectively. The images of $m/e = 82$ and 80 corresponded to the fragment of D elimination, C_6D_5, and the fragment of two D atom (or D_2) elimination, C_6D_4, respectively. Both the images of $m/e = 80$ and 82 contained two components. A line-shape component was superimposed on a disc-like component. The width of the line-shape component changed with the delay time, as illustrated on both wings of figures 3 (*b*) and 3 (*c*), corresponding to the neutral benzene dissociation. The width of the disc-like component did not change with the delay time, as shown in the central parts of figures 3(*b*) and 3(*c*), corresponding to the dissociation from benzene cations. The relative intensity of these two components in the image of $m/e = 80$ depended strongly on the photolysis laser intensity. The photolysis laser intensity dependence shows that the disc-like component located in the centre part resulted from one-photon dissociation, and the line-shape component resulted from two-photon dissociation. On the contrary, the relative intensity of these two components in the image of $m/e = 82$ does not change with the photolysis laser fluence, and they both result from one-photon dissociation.

Figures 4 (*a*) and 4 (*b*) show the images of $m/e = 66$, 64 and 18, corresponding to C_5D_3, C_5D_2 and CD_3. At low photolysis laser intensity, the image of C_5D_3 was disc-like. The photolysis laser intensity dependence shows that the intensity of the disc-like image resulted from one-photon absorption. However, a line-shape image superimposed on the disc-like image was observed at high photolysis laser intensity. The line-shape components of C_5D_3 and C_5D_2 had the same velocity distribution. It indicated that C_5D_2 was due to the fragment cracking of C_5D_3 by photoionization. On the contrary, only the line-shape component was observed in the CD_3 image, resulting totally from the neutral benzene dissociation. The momentum distributions

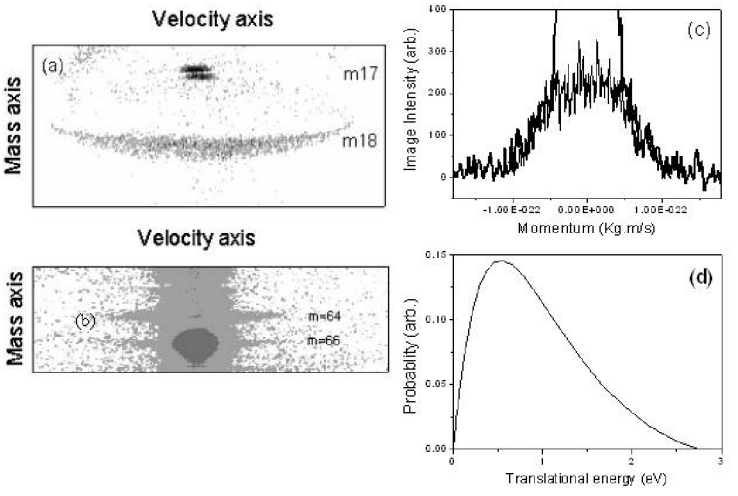

Figure 4. (*a*) Image of $m/e = 18$. The image of $m/e = 17$, corresponding to NH_3, which was used as a mass indicator. (*b*) Images of $m/e = 66$ and 64. (*c*) Momentum distributions of CD_3 and C_5D_3. The momentum of these two fragments match very well, except the central part of C_5D_3, which was obscured by the disc-like image. (*d*) The translational energy distribution for reaction $C_6D_6 \rightarrow C_5D_3 + CD_3$.

of CD_3 and the line-shape component of C_5D_3 match very well, as shown in figure 4(*c*), suggesting that these two fragments resulted from the same dissociation channel. The fragment translational energy distribution is shown in figure 4(*d*). As CD_3 resulted only from the neutral benzene dissociation, measurement of the total CD_3 ion intensity as a function of the photolysis laser fluence revealed the photon number dependence of this dissociation channel. Laser power dependence in the range 1.8–12 mJ cm^{-2} shows that the CD_3 fragments were produced from two-photon absorption. It is interesting to note that the photolysis laser fluence we used in this study is much smaller than that in a previous study [34]. The low laser intensity used in this work allows us to distinguish the one-photon absorption from multiphoton absorption.

Figures 5 (*a*) and 5 (*b*) show the images of masses $m/e = 52$, 54, 56, 30 and 32, corresponding to C_4D_2, C_4D_3 C_4D_4, C_2D_3 and C_2D_4, respectively. C_4D_4 and C_2D_4 had disc-like images, resulting from the dissociative ionization of hot benzene. The image of $m/e = 52$ and 54 had two components; each of them had a line-shape image superimposed on a disc-like image. On the contrary, the image of C_2D_3 only had the line-shape component, resulting totally from neutral hot benzene dissociation. The line-shape components of C_4D_2 and C_4D_3 had the same velocity distribution, indicating C_4D_2 from the fragment cracking of C_4D_3 by photoionization. C_4D_3 has a momentum distribution that matches the momentum distribution of C_2D_3, as shown in figure 5 (*c*), suggesting that these two fragments resulted from the same dissociation channel. The translational energy distribution of this dissociation channel is shown in figure 5(*d*). Measurement of the C_2D_3 ion intensity as a function of photolysis laser fluence in the range 1.8–12 mJ cm^{-2} shows that this fragment resulted from two-photon absorption.

Figure 6 shows the images of mass $m/e = 42$, corresponding to C_3D_3, at various delay times. The image of $m/e = 42$ was disc-like and its width did not change with the delay time. Therefore, it was totally from the dissociation of hot benzene after

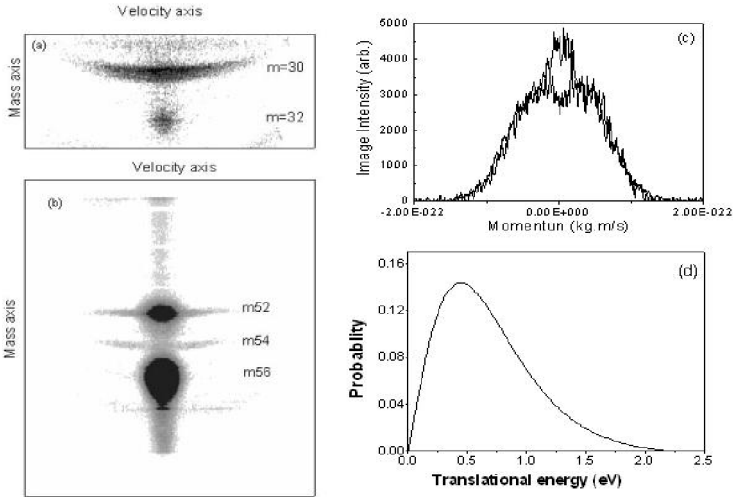

Figure 5. (*a*) Images of $m/e = 32$ and 30. (*b*) Images of $m/e = 56$, 54 and 52. (*c*) Momentum distributions of C_2D_3 and C_4D_3. The momentum of these two fragments match very well, except the central part of C_4D_3, which had an additional contribution from the disc-like image. (*d*) Translational energy distribution for reaction $C_6D_6 \rightarrow C_4D_3 + C_2D_3$.

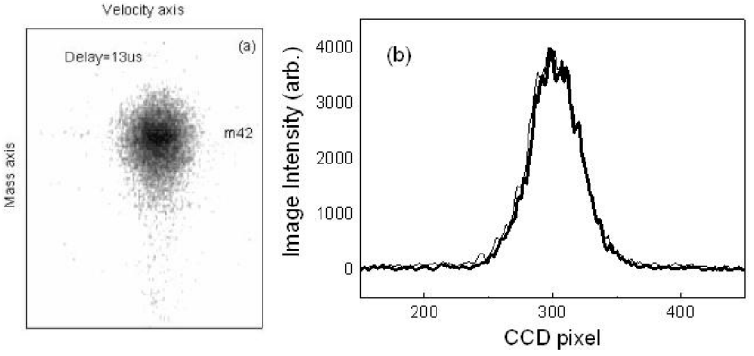

Figure 6. (*a*) Disc-like image of $m/e = 42$. (*b*) Image intensity profiles of the disc-like image at delay times 13 and 32 μs.

the ionization. The measurement of photolysis laser fluence dependence shows that it was from one-photon absorption.

From the observation of the image, we can conclude that H atom elimination is the only one-photon dissociation channel of benzene at 193 nm. Two ring opening channels, $C_6D_6 \rightarrow C_5D_3 + CD_3$ and $C_6D_6 \rightarrow C_4D_3 + C_2D_3$, were observed and confirmed by the momentum match between the fragments in each channel. However, they are from two-photon dissociation. The observation of C_5D_3 and CD_3 fragments confirms the report of the ring-opening channel in the previous study [34].

In order to produce C_5H_3 and CH_3, H atoms in benzene must migrate until one carbon gathers three H atoms and then the C–C bond breaks. This must involve successive H atom migration and benzene isomerization, and the dissociation mechanism must be very complicated. The potential energy surface calculated

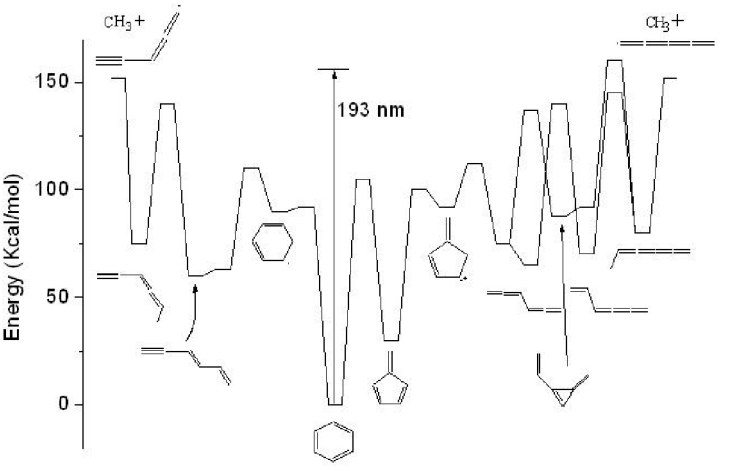

Figure 7. Energy diagram of the ring-opening dissociation $C_6D_6 \rightarrow C_5D_3 + CD_3$ from *ab initio* results. Note that there are many intermediates that can dissociate into $C_4D_3 + C_2D_3$ by a simple C–C bond fission.

by Mebel *et al*. indicates that the ring-opening dissociation of benzene is indeed energetically allowed at 193 nm [35]. Part of the calculated results of the ring-opening dissociation mechanisms is shown in figure 7. The dissociation barrier is very close to the 193 nm photon energy; therefore, the branching ratio of the ring-opening channel from one-photon dissociation is expected to be negligible. Although various dissociation pathways to produce C_5D_3 and CD_3 have been investigated by *ab initio* calculations, no calculation was performed for the $C_6D_6 \rightarrow C_4D_3 + C_2D_3$ dissociation channel. However, as shown in figure 7, most of the calculated dissociation pathways of $C_6D_6 \rightarrow C_5D_3 + CD_3$ have the intermediates that can dissociate into C_4D_3 and C_2D_3 by a simple C–C bond fission. The dissociation of one of the C_6D_6 intermediates could thus also provide a route to branch to the $C_4D_3 + C_2D_3$ product channel. These are the possible dissociation pathways producing C_4D_3 and C_2D_3. The observation of the fragments C_2D_3 and CD_3 from ring-opening dissociation provides a possible explanation of the photodissociation products of methane, ethane, ethylene and acetylene in benzene photolysis at 184.9 nm.

The dissociation rate of $C_6D_6^{\ddagger}$ with internal energy of 147 kcal mol^{-1} from the 193 nm photon excitation was measured from the intensity change of the disc-like image at various delay times. A dissociation rate of $(5 \pm 1) \times 10^4\,s^{-1}$, corresponding to a lifetime of $20 \pm 4\,\mu s$ was obtained from the disc-like image intensity change of $m/e = 42$, 52, 56, 66 and 80, as shown in figure 8. The dissociation rate of $C_6H_6^{\ddagger}$ with the same internal energy was measured from the disc-like image intensity change of $m/e = 52$ and 39. A dissociation rate of $(1 \pm 0.2) \times 10^5\,s^{-1}$, corresponding to a lifetime of $10 \pm 3\,\mu s$, was obtained. However, the intensity of $m/e = 52$ with internal energy of 115 kcal mol^{-1} from the 248 nm photon excitation did not change with the delay time, as shown in figure 8. This is because the lifetime is too long to be measured in our instrument. We estimated the upper limit of the dissociation rate of $C_6H_6^{\ddagger}$ with internal energy of 115 kcal mol^{-1} to be $3 \times 10^3\,s^{-1}$. The dissociation rate of benzene at 193 and 211 nm have been calculated to be 3.6×10^4 and $6 \times 10^2\,s^{-1}$, respectively, using the RRKM model on the electronic ground-state surface [36].

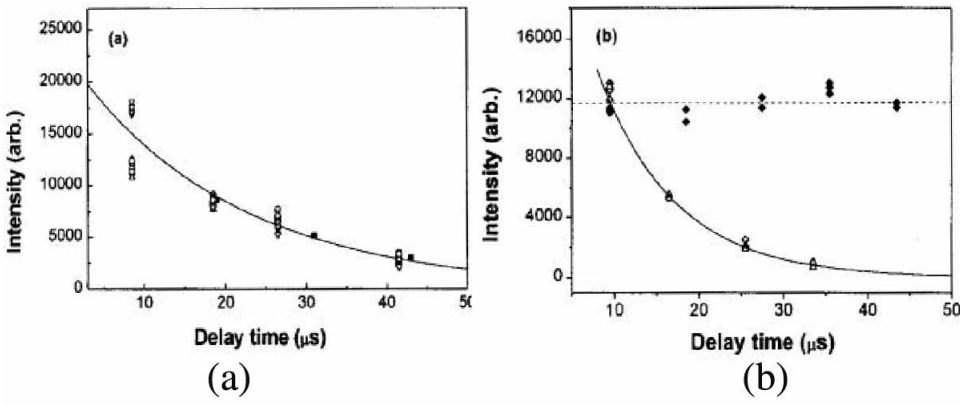

Figure 8. (*a*) The change in disc-like image intensity of $m/e = 42(\circ)$, $52(\nabla)$, $56(\diamond)$, $66(\triangle)$ and $80(\blacksquare)$ as a function of delay time from dissociative ionization of hot C_6D_6 after 193 nm excitation. The solid line shows the fit corresponding to a lifetime of 20 μs. (*b*) The change in disc-like image intensity of $m/e = 52(\triangle)$, $39(\circ)$ as a function of delay time from dissociative ionization of hot C_6H_6 after 193 nm excitation. The solid line shows the fit corresponding to a lifetime of 9.5 μs. Filled diamonds represent the disc-like imaging intensity change of $m/e = 52$ from the hot C_6H_6 after 248 nm excitation. The dashed line represents no intensity change of $m/e = 52$ with delay time.

This shows that the dissociation rate from the RRKM calculation is very close to our experimental measurement.

Although the photon energy of 193 nm is higher than the channel-three threshold (244.5 nm) and the photon energy of 248 nm is lower than the threshold, the fast dissociation rate at 193 nm is not due to the channel-three effect. This is because the non-radiative decay rates above and below the channel-three threshold are much greater than the dissociation rates at 193 or 248 nm. The difference between the dissociation rates at 193 and 248 nm simply reflects the internal energy dependence of the dissociation rate.

3.2. *Fluorobenzene*

UV absorption of the phenyl halides (–Cl, –Br, –I) in the range 190–250 nm corresponds to the excitations of electrons of the phenyl ring and the non-bonding electrons of the halogen atoms. The non-bonding electron excitation of the halogen atoms leads to direct dissociation, that is an immediate release of halogen atoms on a repulsive surface. Alternatively, the excitation of the phenyl ring results in an excited state that is stable with respect to dissociation. Dissociation occurs indirectly either through the coupling of the stable and repulsive state or after the internal conversion from an initial excited state to a lower electronic state. Direct dissociation is fast and releases a large amount of kinetic energy. Indirect dissociation results in a limited release of kinetic energy due to the extensive energy randomization among vibrational degrees of freedom and has a slow dissociation rate. Statistical transition-state theory has predicted that, given comparable pre-exponential factors for different bond fissions, the reaction pathway with the lowest energetic barrier should dominate the indirect dissociation. As the C–X ($X = Cl, Br, I$) bond energy is relatively small, halogen atom elimination is expected to be the major channel in the indirect dissociation. Photodissociation of iodobenzene [37, 38], bromobenzene

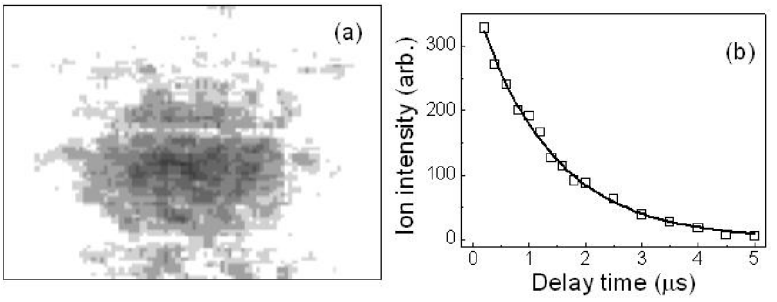

Figure 9. (*a*) Images of $m/e = 70$ ($C_4H_3F^+$). (*b*) Intensity decay of the image as a function of delay time.

[38, 39], chlorobenzene [38, 40–43], *o*-, *m*- and *p*-chlorotoluene [43–46] and *o*-, *m*- and *p*-dichlorobenzene [45, 47, 48] has been studied extensively. Halogen atom elimination was indeed found to be the only dissociation channel, and both direct and indirect dissociation have been observed.

Compared to the other phenyl halides, the photochemistry of the fluorine atom substituted benzenes has received little attention. As the fluorine atom is not an electronic chromophore in the 190–250 nm region, the UV absorption only correlates to excitation of the phenyl ring. Therefore, an immediate release of F atom on a repulsive surface does not occur. In addition, the C–F bond has a very high dissociation threshold and F atom elimination from the ground state after internal conversion is not expected to occur. As a result, neither the direct dissociation nor the indirect dissociation of C–F cleavage is expected. The dissociation mechanism of fluorobenzene in this photon energy region should be very different from those of the other phenyl halides.

Fragment ions of $m/e = 70$, 76 and 95 were observed from the photodissociation of C_6H_5F at 193 nm. Figure 9(*a*) shows the image of $m/e = 70$ ($C_4H_3F^+$). The shape of the image is disc-like; it must therefore result from the dissociation of excited fluorobenzene after ionization. This cation dissociation channel has been observed in previous studies [49, 50]. The dissociation rate of the neutral excited fluorobenzene molecules due to 193 nm photon excitation was measured from the intensity decay of this cation at various delay times. A dissociation rate of $(8 \pm 3) \times 10^5\,s^{-1}$, corresponding to a lifetime of 1.2 μs, was obtained, as shown in figure 9 (*b*).

The fragment ion with $m/e = 76$ ($C_6H_4^+$) has the largest ion intensity. The images at various delay times are shown in figure 10 (*a*). As the delay time between pump and probe laser pulses increased, the length of the image increased rapidly. This is the C_6H_4 fragment that resulted from the dissociation of neutral excited fluorobenzene, corresponding to HF elimination. A dissociation rate of $(1.4 \pm 0.8) \times 10^6\,s^{-1}$ was obtained from the product growth with respect to the delay time between pump and probe laser pulses, as shown in figure 10 (*b*). The similar dissociation rates of $m/e = 70$ and 76 indicate that they must be from the same electronic state. The photofragment translational energy distribution of HF elimination is shown in figure 10 (*c*). The average released translational energy is large, and the maximum translational energy reaches the maximum available energy of the reaction $C_6H_5F \rightarrow C_6H_4 + HF$. As the fragment maximum translational energy corresponds to the products C_6H_4 and HF produced in the ground electronic state, and the

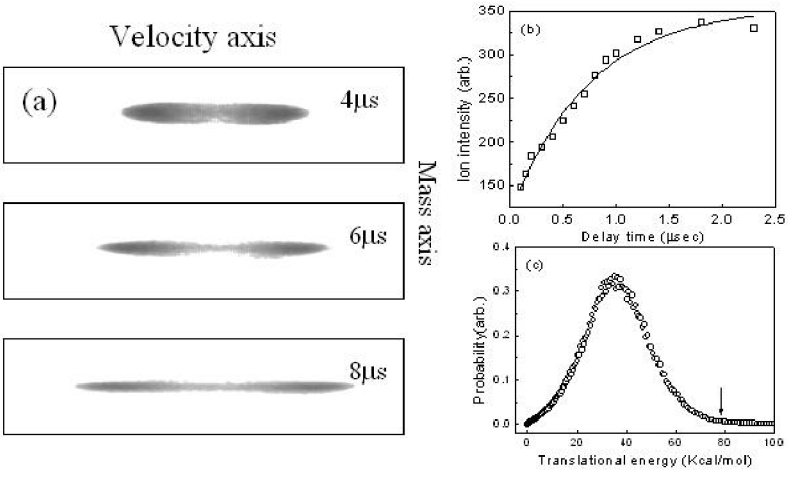

Figure 10. (*a*) Images of $m/e = 76$ ($C_6H_4^+$) at various delay times. (*b*) Product C_6H_4 growth with respect to the delay time between pump and probe pulses. (*c*) Photofragment translational energy distribution of the reaction $C_6H_5F + h\nu_{193\,nm} \rightarrow C_6H_4 + HF$. The arrow indicates the maximum available energy.

ground state of these two closed-shell fragments only correlates to the ground state of the parent molecule, the dissociation must result from the ground electronic state.

In addition, the decay of $m/e = 95$ ($C_6H_4F^+$), corresponding to a dissociation rate of $(7 \pm 2) \times 105\,s^{-1}$, was obtained. The value of the rate indicates that it comes from the same electronic state as that of the HF elimination channel. In fact, a non-zero intensity of $m/e = 95$ ($C_6H_4F^+$) at a long delay time was observed, suggesting the existence of an H atom elimination channel from neutral excited fluorobenzene. However, the fragment ion intensity is very small; 25 times smaller than that of C_6H_4. Although we do not have the ionization cross-sections for these fragments at present, the large difference in the ion intensities between these two fragments indicates that HF elimination is the major channel.

Similar dissociation channels were also observed in the photodissociation of C_6D_5F with small differences in the dissociation rates. A large intensity of fragment ion $m/e = 80$ ($C_6D_4^+$) and a small intensity of ion $m/e = 99$ ($C_6D_4F^+$) were observed, corresponding to a major dissociation channel of DF elimination and a minor dissociation channel of D atom elimination, respectively. The shape of the image $m/e = 73$ ($C_4D_3F^+$) was disc-like, and the dissociation rate obtained from the intensity decay of these disc-like images is $(1.8 \pm 0.5) \times 10^5\,s^{-1}$, that is about four times slower than that of C_6H_5F.

As the photophysics and photochemistry processes of benzene have been studied extensively, it is interesting to compare the photodissociation of fluorobenzene to that of benzene. The ground-state potential energy surface of benzene for various dissociation channels has been calculated by *ab initio* methods [36], as shown in figure 11(*a*). The H-elimination occurs without an intrinsic barrier. The other dissociation channel is the elimination of the hydrogen molecule leading to *o*-C_6H_4. This channel is less endothermic than the H-atom elimination but has a high barrier. The calculation also shows that the transition state for the 1,2-H_2 elimination from benzene converges to the transition state for the three-centre 1,1-H_2

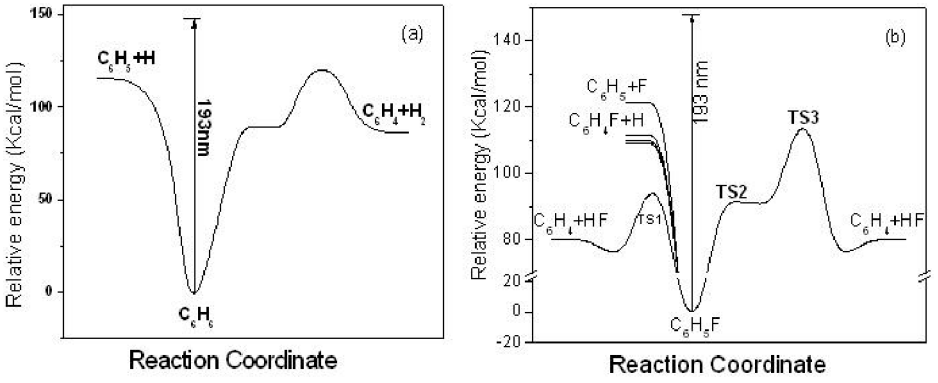

Figure 11. Energy diagrams for isomerization and dissociation reactions of (*a*) benzene and (*b*) fluorobenzene.

elimination and connects the products, *o*-C_6H_4 and H_2. Thus, the H_2-elimination is preceded by the 1,2-H shift and then the three-centre elimination. Although both H-atom and H_2-molecular elimination are energetically possible, H_2-molecular elimination was not observed at 193 nm because of the high barrier.

The fluorobenzene potential energy curves for various dissociation channels obtained by density functional B3LYP/6-31 + G* calculations are shown in figure 11 (*b*). In addition to the F-atom elimination through the C–F bond cleavage, which is illustrated by a high dissociation threshold, the dissociation channels of the H-atom elimination and HF elimination through a three-centre reaction mechanism are very similar to those of the H-atom and H_2-molecule elimination channels in benzene. The H-atom elimination can occur from three positions of the aromatic ring, and results in slightly different energies, as shown in figure 11 (*b*). The three-centre HF elimination starts from the 1,2-H shift through the transition state TS2, and then HF elimination through transition state TS3. However, in contrast to the H_2 four-centre elimination in benzene, the transition state of the HF four-centre elimination in fluorobenzene does *not* converge to that of the three-centre elimination and it has a very low barrier. It is this channel that makes the photodissociation of fluorobenzene very different from that of benzene. The HF bond distance in the transition state TS1 (1.09 Å) is very close to the product's HF bond distance (0.917 Å), compared to the long HF bond distance (1.67 Å) in the transition state TS3. As a result, most of the fluorobenzene dissociates through HF four-centre elimination due to the low barrier height and the kinetic energy released is large because of the late barrier characteristics of the transition state TS1.

We used the potential energy surface obtained from the density functional calculation and performed RRKM calculations for various reaction rates. The rate constant for the product formation from four-centre elimination is $1.1 \times 10^6\,s^{-1}$. For the three-centre elimination, we can use the steady-state approximation (for the intermediate formed after the 1,2-H shift) and calculate the total rate constant for the $C_6H_5F \rightarrow TS2 \rightarrow \text{intermediate} \rightarrow TS3 \rightarrow C_6H_4 + HF$ process. This calculation gives $2.2 \times 10^3\,s^{-1}$, that is the three-centre elimination is much slower than the four-centre elimination. For the C_6D_5F dissociation rate, the RRKM calculation shows that the four-centre DF elimination via TS1 is $2.7 \times 10^5\,s^{-1}$, while the overall rate for the three-centre elimination is $3.65 \times 10^2\,s^{-1}$. Assuming that the four-centre elimination is the dominant reaction process, we calculated the lifetime of C_6F_5F as

0.9 μs and that of C_6D_5F as 3.7 μs. These values are in good agreement with the experimental lifetimes.

3.3. *Toluene and m-xylene*

The UV fluorescence quantum yields of toluene and xylene in the S_1 state decrease rapidly with increasing photon energy [1–5]. For these molecules, the most important monomolecular process after excitation to the S_1 state is photoisomerization with formation of the derivatives of fulvenes, benzvalenes, and prismanes, as well as isomerization with a change of the alkyl substitute's position in the aromatic ring [51–55]. The generally accepted view is that photoisomerization of this kind proceeds by the intermediary formation of isomers like fulvene and benzvalene with their further rearomatization. It has been suggested that all isomerization processes of benzene and its alkyl derivatives can be described in terms of ring permutation [56]. Figure 12 shows some of the ring permutation isomerizations of benzene and xylene. Note that not only the positions of the alkyl groups can be changed during the ring permutation isomerization but also the carbon atoms within the aromatic ring can be exchanged during the ring permutation. One important characteristic of the ring permutation is that the carbon and hydrogen atoms belonging to the alkyl groups are *not* involved in the exchange with those atoms in the aromatic ring. The ring permutation has been observed in benzene and alkyl-substituted benzene in the condensed phase and in the gas phase after excitation to the S_1 state [51, 57, 58].

As the photon energy increases, new isomerization and dissociation channels may open. The ion images of the fragments from the photodissociation of d_3-toluene at 193 nm corresponding to excitation of the S_2 state are shown in figure 13. In addition to the major fragments of $C_6H_5CD_2$, C_6H_5 and CD_3 from the dissociation of $C_6H_5CD_3 \rightarrow C_6H_5CD_2 + D$ and $C_6H_5CD_3 \rightarrow C_6H_5 + CD_3$, observations of the heavy fragments $C_7H_4D_3$, C_6H_4D, $C_6H_3D_2$ and $C_6H_2D_3$, and the corresponding fragment partners CD_2H, CDH_2 and CH_3 suggest the existence of the other dissociation channel, that is isotope exchange prior to dissociation.

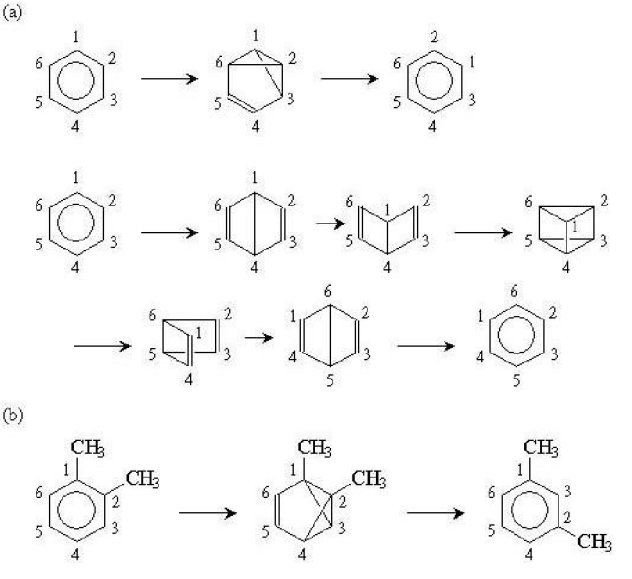

Figure 12. Some of the ring permutations of (*a*) benzene and (*b*) xylene.

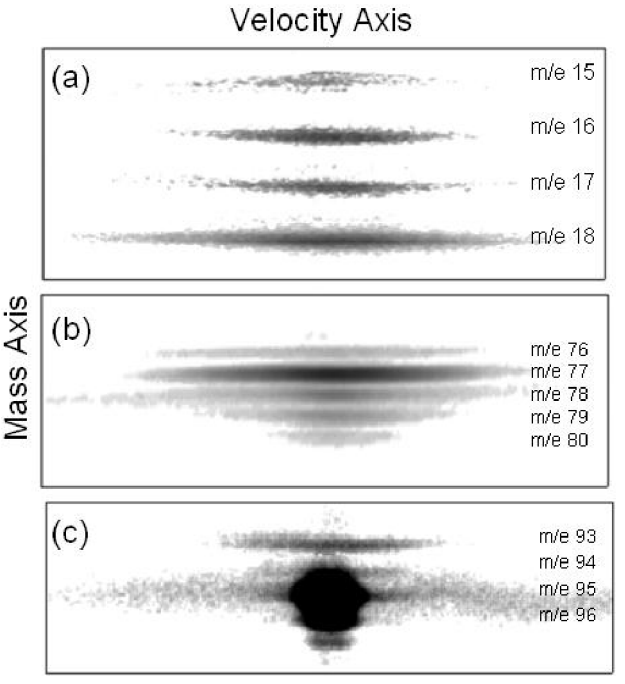

Figure 13. Photofragment ion images of $C_6H_5CD_3$ in three different mass regions. Image of $m/e = 76$ in (*b*) resulted from two-photon dissociation. Parent molecules $m/e = 95$ and $m/e = 96$, 97 due to ^{13}C natural abundance are also shown in image (*c*).

Momentum matches of two fragments in each dissociation channel, as shown in figure 14, further confirm that each fragment pair, C_6H_5 and CD_3, C_6H_4D and CD_2H, $C_6H_3D_2$ and CDH_2, and $C_6H_2D_3$ and CH_3, is from the dissociation of $C_6H_5CD_3$. These momentum matches also exclude the contribution from three-body dissociation, like the dissociation of clusters, or the contribution from cation dissociation. Measurements of the fragment intensities as a function of photolysis laser power in the region 2–50 mJ cm^{-2} show that all of these dissociation channels result from one-photon dissociation. The photodissociation of $C_6H_5{}^{13}CH_3$ was also studied. It shows that in addition to the major dissociation channel, $C_6H_5{}^{13}CD_3 \rightarrow C_6H_5 + {}^{13}CH_3$, the observation of $^{13}CC_5H_5$ and CH_3 indicates that the methyl carbon atom is also involved in the exchange with aromatic carbon atoms prior to dissociation.

The isotope exchange we observed in $C_6H_5CD_3$ and $C_6H_5{}^{13}CH_3$ cannot be explained by the ring permutation. A reasonable isomerization mechanism that explains the experimental results is the isomerization from a six-membered ring (toluene) to a seven-membered ring (cycloheptatriene, CHT). After isomerization to the seven-membered ring, isotopic scrambling of the H/D and carbon atoms occurs through H- or D-atom migration around the seven-membered ring. Finally, the rearomatization of CHT to toluene and the subsequent dissociation through C–C bond cleavage results in the formation of fragments CD_2H, CDH_2 and CH_3, and their heavy fragment partners C_6H_4D, $C_6H_3D_2$ and $C_6H_2D_3$. H- or D-atom elimination can occur from CHT, or after the rearomatization of CHT to toluene.

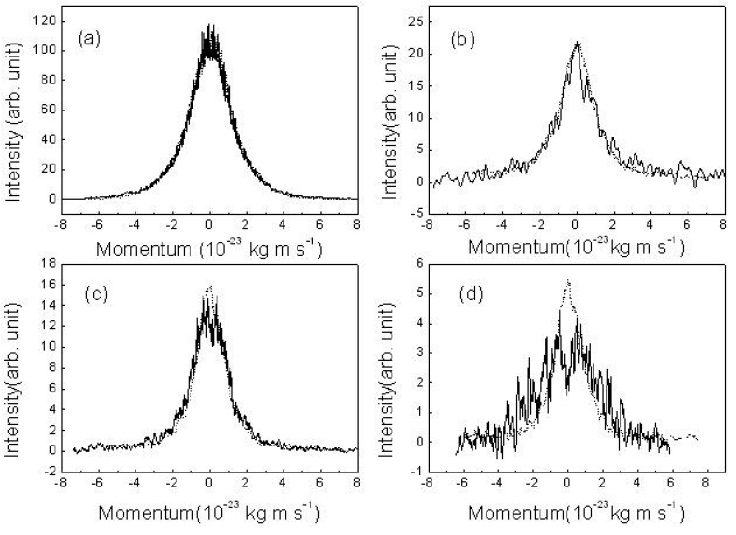

Figure 14. The momentum matches of two fragments in each dissociation channel: (*a*) $m/e = 77$ and 18, (*b*) $m/e = 78$ and 17, (*c*) $m/e = 79$ and 16, (*d*) $m/e = 80$ and 15. The thick lines represent light fragments, and the thin lines represent heavy fragments.

The same mechanism can be used to explain the formation of the respective photofragments CH_3, $^{13}CH_3$, C_6H_5 and $C_5{}^{13}CH_5$ from the dissociation of $C_6H_5{}^{13}CH_3$.

This particular isomerization pathway is supported by *ab initio* calculations. The energies of the dissociation barriers, isomers and various transition states along the isomerization pathway from *ab initio* calculation are shown in figure 15. The dissociation of toluene has barrier heights of 89.7 kcal mol^{-1} for C–H bond cleavage, and 103.8 kcal mol^{-1} for C–C bond cleavage. The six- to seven-membered ring isomerization has a barrier height of 84.9 kcal mol^{-1}. As the barrier heights are all very close in energy, direct C–C and C–H bond dissociation competes with isomerization. Most of the toluene molecules dissociate directly through C–C and C–H bond cleavages after the internal conversion. However, a small fraction of toluene molecules isomerize to CHT. The migration of H or D atoms in CHT due to the low barrier height results in isotopic scrambling of D/H atoms. The comparison between the experimental ratios of various isotope substituted fragments and the statistical ratios indicates that the isotopic scrambling of D/H atoms in CHT is nearly complete prior to rearomatization.

The results of the experiments can be described using the following reactions.

$$C_6H_5CD_3 + h\nu_{193\,nm} \rightarrow C_6H_5CD_3^* \qquad \text{(excitation)} \qquad (5)$$

$$C_6H_5CD_3^* \rightarrow C_6H_5CD_3^{\ddagger} \qquad \text{(internal conversion)} \qquad (6)$$

$$C_6H_5CD_3^{\ddagger} \rightarrow C_6H_5CD_2 + D$$
$$\text{(direct dissociation after internal conversion)} \qquad (7a)$$

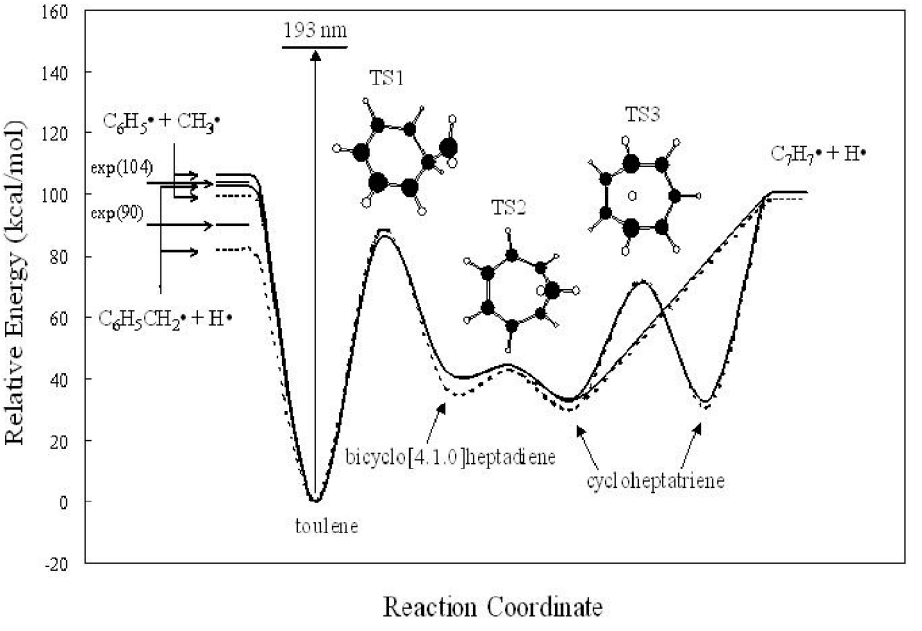

Figure 15. Energy diagram for isomerization and dissociation reactions of toluene. The energies shown are computed at B3LYP/aug-cc-pVTZ (solid line) and CCSD/6-311+G* (dashed line) at the geometry optimized by B3LYP/6-31+G*.

$$C_6H_5CD_3^{\ddagger} \rightarrow C_6H_5 + CD_3 \quad \text{(direct dissociation after internal conversion)} \qquad (7b)$$

$$C_6H_5CD_3^{\ddagger} \rightarrow \text{c-}C_7H_5D_3^{\ddagger} \quad \text{(isomerization)} \qquad (8)$$

$$\text{c-}C_7H_5D_3^{\ddagger} \rightarrow \text{c-}C_7H_5D_3^{\ddagger} \quad \text{(isotopic scrumbling)} \qquad (9)$$

$$\text{c-}C_7H_5D_3^{\ddagger} \rightarrow \text{c-}C_7H_{5-x}D_{2+x} + H(\text{or D}) \quad (x = 0, 1)$$
(seven-membered ring dissociation) (10)

$$\text{c-}C_7H_5D_3^{\ddagger} \rightarrow C_6H_{5-x}D_xCH_xD_{3-x}^{\ddagger} \ (x = 0, 1, 2, 3) \quad \text{(rearomatization)} \qquad (11)$$

$$C_6H_{5-x}D_xCH_xD_{3-x}^{\ddagger} \rightarrow C_6H_{5-x}D_xCH_{x-1}D_{3-x} + H \quad (x = 1, 2, 3)$$
$$\text{or} \quad C_6H_{5-x}D_xCH_xD_{3-x-1} + D \quad (x = 0, 1, 2)$$
(dissociation after rearomatization) (12a)

$$C_6H_{5-x}D_xCH_xD_{3-x}^{\ddagger} \rightarrow C_6H_{5-x}D_x + CH_xD_{3-x} \quad (x = 0, 1, 2, 3)$$
(dissociation after rearomatization) (12b)

All of the dissociation products from reactions (7), (10) and (12) were ionized by VUV laser and detected by the ion image detector. They can be represented by the following reaction:

$$P + h\nu_{VUV} \rightarrow P^+ \quad (P = C_6H_{5-x}D_x, CH_xD_{3-x}, C_7H_5D_2, C_7H_4D_3) \tag{13}$$

However, at very short delay times, some of the hot toluene that has not dissociated into fragments could absorb the VUV photon resulting in dissociative ionization.

$$C_6H_5CD_3^{\ddagger} + h\nu_{VUV} \rightarrow C_6H_{5-x}D_xCH_{x-1}D_{3-x}^+ + H + e^- \quad (x = 1, 2, 3)$$
$$\text{or } C_6H_{5-x}D_xCH_xD_{3-x-1}^+ + D + e^- \quad (x = 1, 1, 2) \tag{14}$$

$$C_6H_5CD_3^{\ddagger} + h\nu_{VUV} \rightarrow C_6H_{5-x}D_x^+ + CH_xD_{3-x} + e^- \quad (x = 1, 1, 2, 3) \tag{15}$$

The ions from the dissociative ionization channels produce the disc-like image at short delay times. However, at long delay times, most of the hot toluene dissociates into fragments, and this background decays to zero. The dissociation lifetime, $1/k_7$ $[= 1/(k_{7a} + k_{7b})] = 850$ ns at 193 nm, is very short compared to the delay time between pump and probe laser pulses ($\sim$30 μs) in imaging experiments, and therefore most of the hot toluene molecules dissociate into fragments and only the line-shape images were observed.

The product build-up times of the respective photofragments C_6H_5, C_6H_4D, $C_6H_3D_2$, $C_6H_2D_3$, $C_7H_5D_2$ and $C_7H_4D_3$, originating from $C_6H_5CD_3$, were measured by a TOF mass spectrometer. The results are shown in figure 16. The non-zero intensity at $t = 0$ and the intensity decay of $m/e = 94$ in figure 16 is due to the background from the dissociative ionization channels. Reactions (7)–(14) are used to simulate the apparent rate and the relative intensities of the fragments. We neglect all the isotopic effects except those on the H- and D-atom elimination channels (reactions 7a and 12a), for which the isotopic effect is expected to be large. We assume that $k_8 = k_{-11}$, $k_{11} = k_{-8}$, $k_9 = k_{-9}$ and $k_{7b} = k_{12b}$. The simulation results are shown in figure 16. From the simulation, we obtain

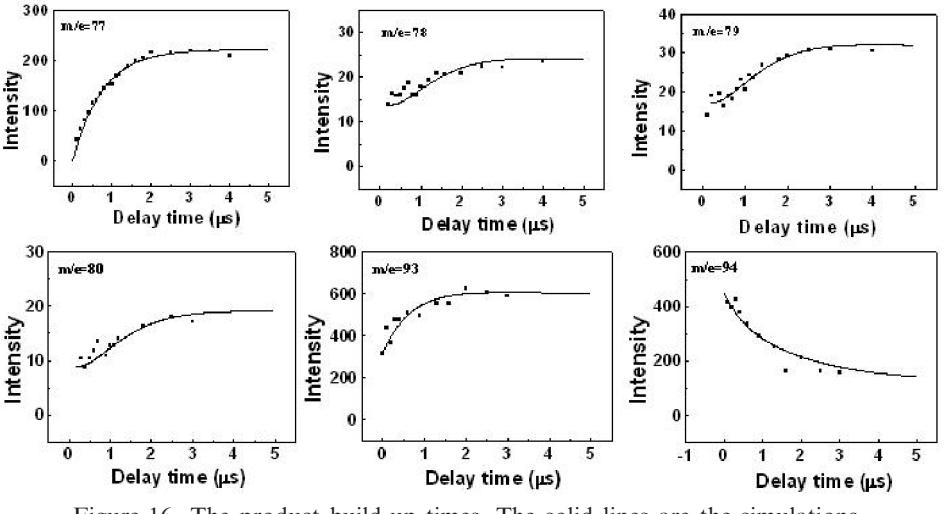

Figure 16. The product build-up times. The solid lines are the simulations.

k_7 $(=k_{7a}+k_{7b})=(1.17\pm0.08)\times10^6\,s^{-1}$, $k_8=(3.4\pm0.3)\times10^5\,s^{-1}$, $k_9>5\times10^8\,s^{-1}$, $k_{10}<1\times10^7\,s^{-1}$ and $k_{11}=(1\pm0.3)\times10^8\,s^{-1}$ and the ratio of H- and D-atom elimination from the methyl group of toluene is 1.6 ± 0.2. Values for k_7, k_9 and k_{11} are very close to those from previous studies of toluene [59–61] and CHT [62, 63]. Although the upper limit of the dissociation rate from the seven-membered ring is larger than the dissociation rate from the six-membered ring, the dissociation from the seven-membered ring must compete with the rearomatization process. As the rearomatization rate is at least 10 times larger than the upper limit of the seven-membered ring dissociation rate, it is not likely that the dissociation from the seven-membered ring is important. The $k_8/(k_7+k_8)$ ratio shows that about $25\pm4\%$ of hot toluene molecules isomerize to CHT, followed by H- and D-atom exchange in CHT, and subsequent rearomatization to toluene prior to dissociation.

Similar isomerization was also observed in *m*-xylene after excitation by 193 nm photons. Figure 17 depicts the photofragment ion images obtained from the photodissociation of d_6-, *m*-xylene at 193 nm. Ions of $m/e=18$, 17 and 16 corresponding to fragments CD_3, CD_2H and CDH_2, respectively, were observed. They have line-shape images. However, the images of the heavy fragments, $C_8H_4D_5$, $C_8H_3D_6$, $C_7H_4D_3$, $C_7H_3D_4$ and $C_7H_2D_5$ have two components. A disc-like component superimposes on a line-shape component at the centre. The line-shape components are the fragments that result from the dissociation of neutral parent molecules. The disc-like images are from the dissociative ionization of undissociated hot xylene by VUV photoionization due to the slow dissociation rate of xylene at 193 nm. The results show that, in addition to the major fragments from the dissociation channels 1,3-$C_6H_4CD_3CD_3\rightarrow C_6H_4CD_3CD_2+D$

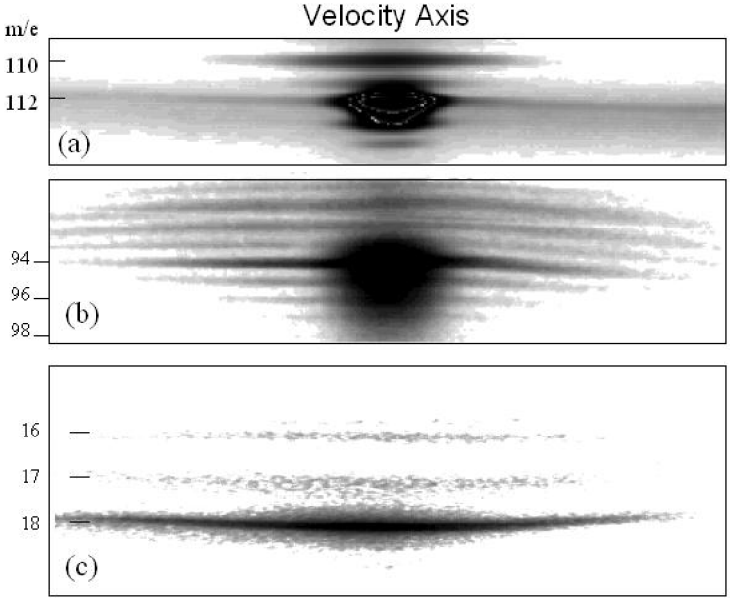

Figure 17. (*a*) Photofragment ion images of $m/e=110$ and 111. The images of the parent molecular ion ($m/e=112$) and its ^{13}C isotopes are also shown. The total delay time is 90 μs. (*b*) Photofragment ion images of $m/e=94$, 95, 96 and 97. The total delay time is 55 μs. Images of $m/e=90$–93 result from multiphoton dissociation. (*c*) Photofragment ion images of $m/e=18$, 17 and 16. The total delay time is 15 μs.

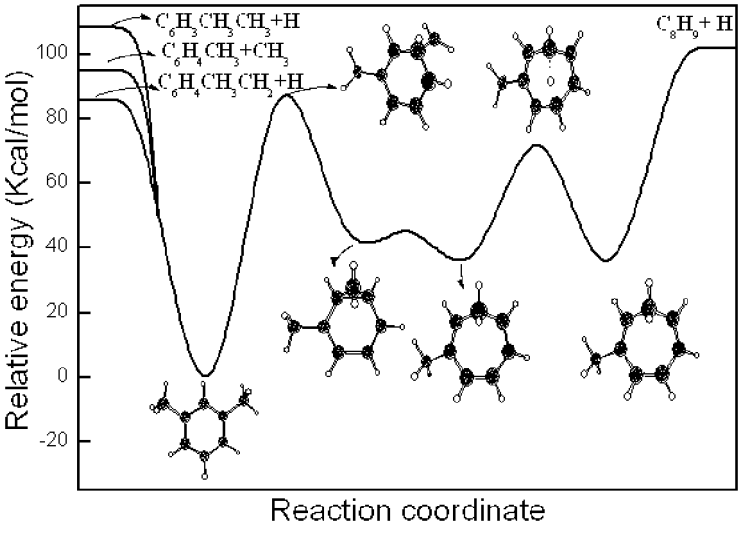

Figure 18. Energy diagram of xylene from *ab initio* calculation (B3LYP/6-31 + G*).

and 1,3-$C_6H_4CD_3CD_3 \rightarrow C_6H_4CD_3 + CD_3$, observation of the heavy fragments $C_7H_3D_4$, $C_7H_2D_5$ and C_7HD_6, and some of the corresponding light fragment partners CD_2H and CDH_2, suggests that a small fraction of xylene molecules undergoes isotope exchange prior to dissociation.

We also performed *ab initio* calculations to obtain the energies of isomers and various transition states along the isomerization and dissociation pathway of *m*-xylene in the ground electronic state. The results are shown in figure 18. The dissociation of xylene has barrier heights of 85 kcal mol^{-1} for C–H bond cleavage from the methyl group, and 96 kcal mol^{-1} for C–C bond cleavage. The six- to seven-membered ring isomerization has a barrier height of 87 kcal mol^{-1}. These barrier heights are all very close in energy. Experimental measurement shows that most of the xylene molecules dissociate directly through C–C and C–H bond cleavage after the internal conversion. However, more than 12% of *m*-xylene molecules isomerize to methyl-CHT, followed by H/D exchange in methyl-CHT and rearomatization prior to dissociation.

Although the seven- (CHT) to six-membered ring (toluene) isomerization was observed experimentally more than four decades ago [64, 65], the reverse reaction was not reported. This is probably because the reverse reaction has a higher activation energy, resulting in a smaller isomerization rate. This isomerization channel has to compete with fast dissociation channels, and therefore isomerization would not be easily observed. As a result, the dissociation mechanism of toluene and xylene after 193 nm excitation has been interpreted as direct C–H or C–C bond cleavage after internal conversion. In this work, we demonstrate that the isomerization from the six- to the seven-membered ring also competes with the direct dissociation in the ground state. This is the first time that this kind of isomerization has been observed experimentally in aromatic molecules. The most significant difference of this particular isomerization channel from the other aromatic isomerization pathways is that alkyl carbon and hydrogen atoms are involved in the exchange with those atoms in the aromatic ring during this isomerization process. This is unlike

that found in ring permutation isomerization, in which only the hydrogen and carbon atoms of the aromatic ring are involved in the exchange.

3.4. *Ethylbenzene and propylbenzene*

For the photodissociation of ethylbenzene at 193 nm (S_2 state), the dominant channel is the C–C bond cleavage. A CH_3 yield of $96 \pm 4\%$ and a dissociation rate of $2 \times 10^7\,s^{-1}$ were reported [59, 60, 66–72]. The dissociation channel due to the H-atom elimination was also observed [59]. Ethyl radical elimination was found to be the major channel for the photodissociation of *n*-propylbenzene at 193 nm, and the dissociation rate is $7 \times 10^6\,s^{-1}$. A dissociation mechanism through internal conversion to S_0 was used to interpret the dissociation rates and branching ratios of xylene, ethylbenzene, *n*-propylbenzene, isopropylbenzene, butylbenzene and trimethylbenzene at 193 and 157 nm [59, 60, 67–72]. No dissociation experiment has been performed for these molecules in the S_1 state. However, the onset and ultimate dominance of IVR in these molecules as the alkane chain is increased was found in the single vibronic level fluorescence spectra of the S_1 state [7]. More recent high-resolution laser fluorescence excitation spectra near the band origin of the S_1 state showed that propylbenzene and butylbenzene exhibit the excess linewidths, but the source of the excess width remains elusive [73].

We have studied the photodissociation of ethylbenzene, d_{10}-ethylbenzene and propylbenzene at both 193 and 248 nm using multimass ion imaging techniques. Figures 19 and 20 depict the photofragment ion images obtained from the photodissociation of ethylbenzene and propylbenzene at 193 nm, and also the fragment translational energy distributions obtained from the ion images. The monotonic decrease in probability with increasing translational energy is a typical characteristic of dissociation from a molecule undergoing internal conversion to the ground electronic state with no exit barrier.

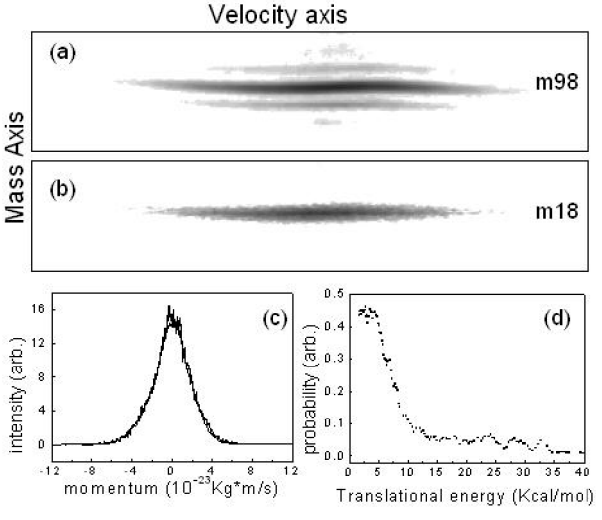

Figure 19. Ion image of photofragments (*a*) $m/e = 98$ and (*b*) $m/e = 18$ from photodissociation of d_{10}-ethylbenzene at 193 nm. The delay times between pump and probe laser pulses are 30 and 7 μs, respectively. (*c*) The translational momentum distributions of $m/e = 18$ (thin solid line) and 98 (thick solid line). (*d*) The fragment translational energy distribution for the reaction $C_6D_5C_2D_5 \rightarrow C_6D_5CD_2 + CD_3$.

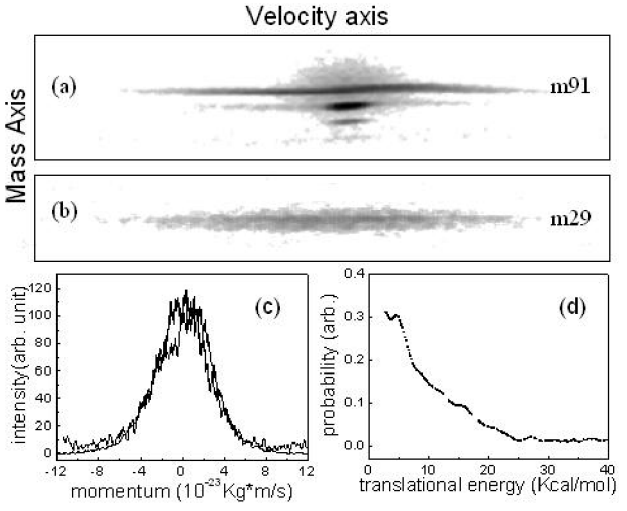

Figure 20. Ion image of photofragment (*a*) $m/e = 91$ and (*b*) $m/e = 29$ from photodissociation of *n*-propylbenzene at 193 nm. The delay times between pump and probe laser pulses are 28 and 8 μs, respectively. (*c*) The translational momentum distributions of $m/e = 29$ (thin solid line) and 91 (thick solid line). (*d*) The fragment translational energy distribution for the reaction $C_6H_5C_3H_7 \rightarrow C_6H_5CH_2 + C_2H_5$.

The photofragment ion images of ethylbenzene obtained at 248 nm are different from those obtained at 193 nm. Figures 21 (*a*) and 21 (*b*) illustrate the ion images of the phenyl radical obtained from the photodissociation of ethylbenzene at 248 nm at two different delay times. They clearly show that the image of fragment $m/e = 91$ has three components: a line-shape component located on both wings, and the other line-shape component superimposed on a disc-like component at the centre. As the delay time between the pump and the probe laser pulses was increased, the component on both wings moved rapidly towards the outside, and the length of the line-shape component at the centre increased. On the contrary, the size of the disc-like image did not change, but the intensity decreased with the increase in the delay time. These three components can be assigned easily according to the relationship illustrated in figure 2. The component on the wings and the line-shape component at the centre are the phenyl radical fragments produced from the dissociation of ethylbenzene with large recoil velocity and small recoil velocity, respectively. The third component, the disc-like image, results from the dissociative ionization of undissociated hot ethylbenzene by VUV photoionization due to the slow dissociation rate at 248 nm.

Among these three components, the decay rate of the disc-like component was found to be $1.1 \times 10^5\,s^{-1}$, as illustrated in figure 21(*c*). The product growth rates of the phenyl radical with large and small recoil velocity components were obtained by forward convolution simulation from the images at various delay times. They show that the product growth rate of the large recoil velocity component is faster than $1 \times 10^6\,s^{-1}$, and that of the small velocity component is $1 \times 10^5\,s^{-1}$. The photofragment translational energy distribution obtained from the line-shape components by forward convolution is shown in figure 21(*d*). The different dissociation rates suggest that there are two mechanisms involved in the dissociation of ethylbenzene

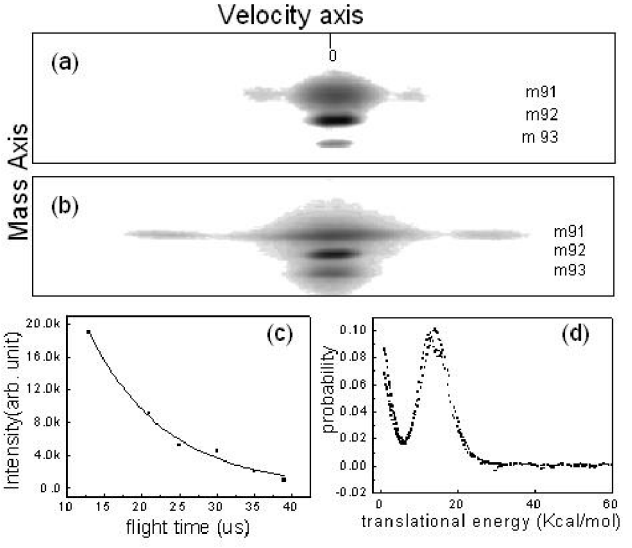

Figure 21. The ion image of the phenyl radical obtained from the photodissociation of ethylbenzene at 248 nm at delay time of (*a*) 15 μs, (*b*) 32 μs. (*c*) Intensity decay of the disc-like image as a function of delay times. A decay rate of $10^5\,s^{-1}$ was obtained. (*d*) The fragment translational energy distribution for the reaction $C_6H_5C_2H_5 \rightarrow C_6H_5CH_2 + CH_3$.

at 248 nm. For the component of small recoil velocity, the average translational energy release is small and the dissociation rate is slow. These are the characteristic of dissociation from the ground electronic state. By contrast, the dissociation rate for the component of large recoil velocity is fast, the average released translational energy is large, and the peak of the distribution is located at 18 kcal mol^{-1}. These are the characteristic of dissociation from a repulsive excited state, or dissociation from an electronic state with an exit barrier. Similar results were obtained for the photodissociation of d_{10}-ethylbenzene and *n*-propylbenzene. Figure 22 shows the results of *n*-propylbenzene. The intensity decay rate of the disc-like image was found to be $4.9 \times 10^4\,s^{-1}$, and two components in translational energy distribution were observed. The product growth rates obtained from simulation are $5 \times 10^4\,s^{-1}$ and greater than $5 \times 10^5\,s^{-1}$ for the slow and fast recoil velocity components, respectively.

A photolysis laser intensity dependence study was carried out in the region 0.7–10 mJ cm^{-2} for 193 nm and 2.2–33 mJ cm^{-2} for 248 nm. The shapes of the translational energy distribution do not change with photolysis laser intensity. The measurements suggest that they all result from one-photon dissociation.

As the ethyl and propyl groups are not the electronic chromophores at 248 nm, the photon absorption corresponds to the excitation of the phenyl ring. Dissociation must occur indirectly either through coupling between the stable and repulsive states or after the internal conversion from the initially excited state to a lower electronic state. Figure 23 shows the potential energy diagram of the reaction $C_6H_5C_2H_5 \rightarrow C_6H_5CH_2 + CH_3$ obtained from *ab initio* calculation (B3LYP/6-31 + G*). In the ground electronic state, the methyl group changes gradually from pyramidal to planar geometry as the C–C bond length increases during the dissociation process. There is no exit barrier for the dissociation from the

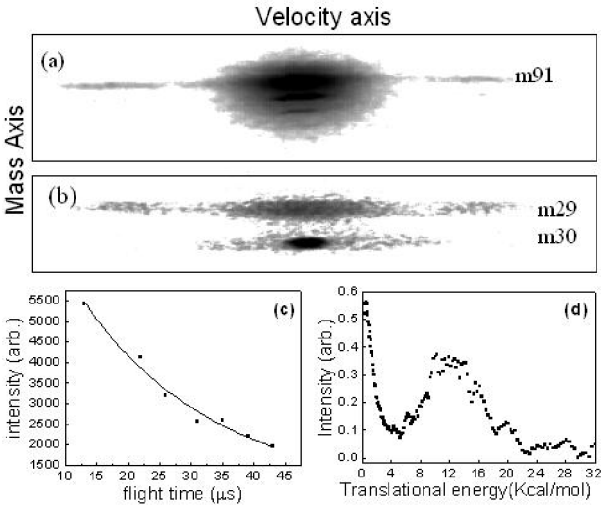

Figure 22. Ion image of photofragments (*a*) $m/e = 91$ and (*b*) $m/e = 29$ from photodissociation of propylbenzene at 248 nm. The delay times between pump and probe laser pulses are 20 and 5 μs, respectively. The image of $m/e = 30$ is the mass indicator.

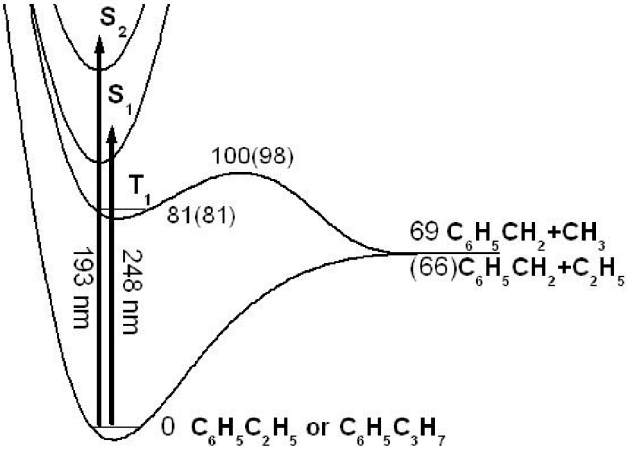

Figure 23. The S_0 and T_1 state energy diagrams of reactions of $C_6H_5C_2H_5 \rightarrow C_6H_5CH_2 + CH_3$ and $C_6H_5C_3H_7 \rightarrow C_6H_5CH_2 + C_2H_5$ obtained by *ab initio* calculation. The numbers are the zero-point energies (kcal mol^{-1}) for the S_0 state, the T_1 state, the transition state and the products. The numbers in parentheses are the energies of propylbenzene.

ground state. This indicates that the slow component in the translational energy distribution results from ground-state dissociation and the fast component does not result from ground-state dissociation. Figure 23 also shows the potential energy diagram in the first triplet state for the same dissociation channel. The exit barrier height is about 31 kcal mol^{-1}. Similar potential energy diagrams were found in the photodissociation channel of *n*-propylbenzene; the corresponding calculated energies for *n*-propylbenzene are shown in parentheses in figure 23. The dissociation from the ground state is barrierless. However, the dissociation from the first triplet state has

a barrier height of 32 kcal mol^{-1}. Although the other electronic states cannot be definitively excluded (no potential energy surfaces for the other excited states are available), the exit barrier in the first triplet state and the translational energy distribution of the fast component in both ethylbenzene and propylbenzene suggest that dissociation upon intersystem crossing to the first triplet state is a likely explanation for the fast component in the translational energy distribution of ethylbenzene and *n*-propylbenzene.

Two-colour photoionization has been applied to the measurement of the time evolution of the laser-excited first singlet state of benzene, toluene, ethylbenzene and xylene [4, 74, 75]. The observed photoionization signals exhibited a biexponential dependence upon the time delay between the pump and ionization lasers. The fast exponential decay resulted from the relaxation of the S_1 state, and the slow exponential decay was interpreted as the decay of the T_1 state after the $S_1 \rightarrow T_1$ intersystem crossing. Although the triplet state was found to play an important role in the relaxation of the S_1 state in these molecules, the interpretation of the T_1 state decay was only attributed to the intersystem crossing from the T_1 to the S_0 state. No dissociation from the T_1 state following the excitation of the first singlet state has been reported. In those studies, the decay rates were monitored as a function of vibrational energy and were found to increase with energy. For ethylbenzene, the decay rate of the triplet state was found to be 4×10^5 s^{-1} at the excitation wavelength of 266 nm [4]. In this work, the excitation energy is larger than the energy found in a previous study, and the increase in the decay rate is therefore expected. However, additional channels may open up as the energy increases and result in competition with intersystem crossing from the T_1 to the S_0 state. Our experimental results demonstrate that the dissociation not only competes with the intersystem crossing but also becomes the dominant channel at the excitation wavelength of 248 nm.

The dissociation of ethylbenzene and *n*-propylbenzene from the S_0 state could result from the direct internal conversion of $S_1 \rightarrow S_0$ or through the two-step intersystem crossing $S_1 \rightarrow T_1 \rightarrow S_0$. Therefore, the minimum values of 0.75 and 0.8 for the intersystem crossing quantum yields of ethylbenzene and propylbenzene, respectively, were obtained from the ratio of the fast and slow components in the translational energy distribution. The high intersystem crossing quantum yield indicates the strong coupling between the S_1 and T_1 states at this energy. This is the first time that the dissociation of alkylbenzenes from the triplet state has been observed. The results suggest that dissociation from the first triplet state may play a very important role in the photoexcitation of alkylbenzenes in the S_1 state.

3.5. *Chlorotoluene*

Although photodissociation of haloaromatic compounds has been studied extensively in a molecular beam [37–48], halogen atom elimination was found to be the only dissociation channel in previous studies. As the excitation of haloaromatic compounds by 193 nm photons corresponds not only to the excitation of non-bonding electrons of halogen atom but also to the excitation of electrons of the phenyl ring, a hot molecule dissociation mechanism must play an important role in these molecules due to the rapid internal conversion from the phenyl ring excitation. Dissociation channels with low barrier heights might occur in these hot molecules.

For chlorotoluene, dissociation channels other than Cl-atom elimination may be opened up because the bond energies of $CH_3C_6H_4$–Cl, $C_6H_4ClCH_2$–H and

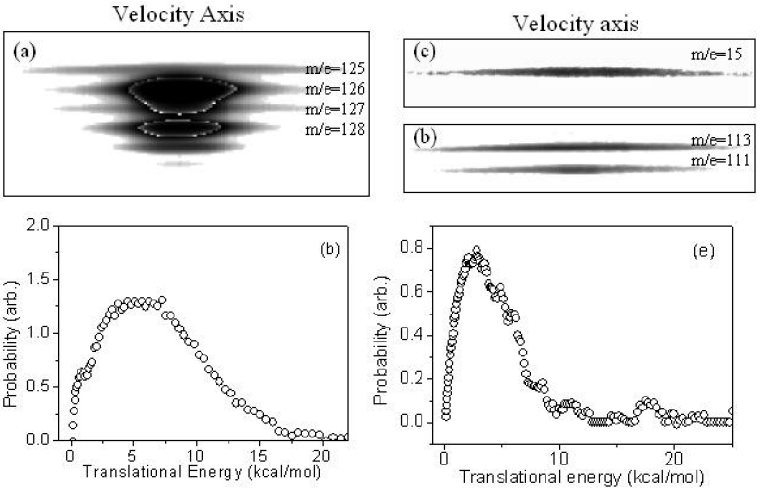

Figure 24. (*a*) Images of $m/e = 125$–129. (*b*) Photofragment translational energy distribution of reaction $p\text{-}C_6H_4ClCH_3 \rightarrow C_6H_4ClCH_2 + H$. (*c*) Image of $m/e = 15$. (*d*) Images of $m/e = 111$, 113. (*e*) Photofragment translational energy distribution of reaction $p\text{-}C_6H_4ClCH_3 \rightarrow C_6H_4Cl + CH_3$.

$C_6H_4Cl\text{-}CH_3$ are very close. In addition to the Cl-atom elimination, dissociation channels were indeed observed in our study [20]. Figure 24(*a*) illustrates the images of $m/e = 125$–129 from the photodissociation of *p*-chlorotoluene. Images of $m/e = 126$ and 128 are the parent molecules $C_6H_4ClCH_3$ of isotopes ^{35}Cl and ^{37}Cl, respectively. $m/e = 129$ is the ^{13}C isotope of the parent molecule. Images of $m/e = 125$ and 127 are photofragments $C_6H_4{}^{35}ClCH_2$ and $C_6H_4{}^{37}ClCH_2$, respectively, resulting from H-atom elimination. The translation energy distribution, as illustrated in figure 24 (*b*), shows that the average translational energy released is small and the maximum translational energy is much less than the available energy. Figures 24 (*c*) and 24 (*d*) show the images of $m/e = 111$, 113 and 15, corresponding to the photofragments of $C_6H_4{}^{35}Cl$, $C_6H_4{}^{37}Cl$ and CH_3 from the reaction $C_6H_4ClCH_3 \rightarrow C_6H_4Cl + CH_3$. The translational energy distribution, as illustrated in figure 24 (*e*), shows similar properties to those of the H-atom elimination channel. These are typical characteristics of the indirect dissociation from a molecule undergoing internal conversion to a lower electronic state with no exit barrier. Measurement of these fragment ion intensities as a function of photolysis laser fluence in the region 0.14–5.9 mJ cm^{-2} shows that they all resulted from one-photon absorption.

The fragment ion intensity ratios between $C_6H_4ClCH_2$, $C_6H_4CH_3$, C_6H_4Cl and CH_3 from the photodissociation of *p*-chlorotoluene are 0.2 : 1.0 : 0.03 : 0.01. These values have been corrected for the fragment velocity effect. The branching ratios can be obtained directly from the normalization of these values by the ionization cross-sections at this wavelength. The relative branching ratio of the Cl and CH_3 elimination was estimated to be $1 : 0.07 \pm 0.05$. Although we do not have the ionization cross-sections to estimate the branching ratio for the H-atom elimination channel, the relatively large ion intensity ratio between $C_6H_4ClCH_2$ and $C_6H_4CH_3$ suggests that H-atom elimination must also play an important role in the photodissociation of *p*-chlorotoluene.

The dissociation rate of *p*-chlorotoluene was measured from the product growth as a function of delay time between pump and probe laser pulses. A value of $(1.2 \pm 0.2) \times 10^6\,s^{-1}$ was obtained from the growth of fragments $m/e = 15$, 111 and 125, indicating that they all resulted from the same electronic state. The small translational energy released and slow dissociation rate suggest that the dissociation probably occurs in the ground electronic state.

We used the potential energy surface obtained from *ab initio* calculation and performed variational RRKM calculations for various reaction rates of *p*-chlorotoluene. The geometry optimization and vibrational frequencies of the reactants, transition states and products were calculated at the B3LYP/6-311 + G(d, p) level. The calculated bond energies are 90.7, 86.4 and 99.0 kcal mol^{-1} for $CH_3C_6H_4$-Cl, $C_6H_4ClCH_2$-H and C_6H_4Cl-CH_3, respectively. The results of the RRKM calculations show that the dissociation rates for Cl, H and CH_3 eliminations in the ground state are 1×10^6, 7×10^4 and $5 \times 10^5\,s^{-1}$, respectively. The total dissociation rate from the calculation was found to be close to the experimental values, although it overestimates the CH_3 elimination channel.

Compared to most of the previous studies, which focused on the dissociation mechanism of Cl-atom elimination and for which only Cl-atom elimination channel was reported, our experiments demonstrated the existence of other dissociation channels. Although H and CH_3 eliminations are not the major channels, they cannot be neglected. In fact, the similar dissociation products and fragment intensities from H-atom and CH_3 eliminations were also observed in *m*- and *o*-chlorotoluene. However, as the C–I and C–Br bond energies are much smaller than that of the C–Cl bond, halogen atom eliminations are expected to be more competitive in iodotoluene and bromotoluene than in chlorotoluene. Therefore, the H and CH_3 eliminations must be less important in these molecules.

4. Summary

Different substitutions in aromatic molecules show different isomerization and dissociation channels. These substitutions lead to a rich variety of aromatic photochemistry. However, it is interesting to note that at higher excitation energies, the generation of hot molecules for most of the aromatic molecules we studied becomes important because of rapid internal conversion. Dissociation in the ground electronic state therefore plays an important role for these aromatic molecules in the gas phase. This is different from the photochemistry in the condensed phase or in a high-pressure gas because of their rapid energy transfer to the surrounding molecules. As the phenyl ring is a very stable structure, no ring-opening dissociation has been observed at photon energies as high as 6.4 eV. Instead, dissociation reactions through these substitutions and isomerization are the dominant processes. These isomerization and dissociation reactions in the ground electronic state are standard unimolecular reactions. They can be characterized by the ground-state potential energy surface and RRKM calculations. Nowadays the potential energy surface of the ground electronic state can be obtained from *ab initio* calculation with reasonable accuracy. It provides helpful information about the isomerization and dissociation barriers and possible dissociation mechanism. However, it is not straightforward to find all the possible isomerization pathways and dissociation channels from calculation alone because of the large number of atoms in these aromatic molecules. As a result, experimental studies play a very important role in the study of

photodissociation of large molecules, such as aromatic compounds. Special experimental methods, like the multimass ion imaging technique we have demonstrated in this review, together with *ab initio* calculation of the potential energy surface, are expected to continue to provide essential information for the investigation of the photodissociation of aromatic molecules.

Acknowledgements

This work was supported by the National Science Council, Taiwan, under contract NSC 92-2113-M-001-015.

References

[1] C. E. Otis, J. L. Knee, and P. M. Johnson, J. Chem. Phys. **78**, 2091 (1983).
[2] N. Nakashima and K. Yoshihara, J. Chem. Phys. **77**, 6040 (1982).
[3] M. Sumitani, D. V. O'Connor, Y. Takagi, N. Nakashima, K. Kamogawa, Y. Udagawa, and K. Yoshihara, Chem. Phys. **93**, 359 (1985).
[4] M. A. Duncan, T. G. Dietz, M. G. Liverman, and R. E. Smalley, J. Phys. Chem. **85**, 7 (1981).
[5] M. Suto, X. Wang, J. Shan, and L. C. Lee, J. Quant. Spectrosc. Radiat. Transfer **48**, 79 (1992).
[6] S. A. Lee, J. Chem. Phys. **68**, 602 (1977).
[7] J. B. Hopkins, D. E. Powers, and R. E. Smalley, J. Chem. Phys. **72**, 2905 (1980); J. Chem. Phys. **72**, 5039 (1980); J. B. Hopkins, D. E. Powers, S. Mukamel, and R. E. Smalley, J. Chem. Phys. **72**, 5049 (1980); J. B. Hopkins, D. E. Powers, and R. E. Smalley, J. Chem. Phys. **73**, 683 (1980); S. Mukamel, and R. E. Smalley, J. Chem. Phys. **73**, 4156 (1980).
[8] S. T. Tsai, C. K. Lin, Y. T. Lee, and C. K. Ni, Rev. Sci. Instrum. **72**, 1963 (2001).
[9] C. L. Huang, Y. T. Lee, and C. K. Ni, in *Modern Chemical Reaction Dynamics: Experiment and Theory*, edited by K. Liu and X. Yang (World Scientific Publisher, Singapore, 2004).
[10] S. T. Tsai, C. K. Lin, Y. T. Lee, and C. K. Ni, J. Chem. Phys. **113**, 67 (2000).
[11] S. T. Tsai, Y. T. Lee, and C. K. Ni, J. Phys. Chem. A **104**, 10125 (2000).
[12] S. T. Tsai, C. L. Huang, Y. T. Lee, and C. K. Ni, J. Chem. Phys. **115**, 2449 (2001).
[13] C. L. Huang, J. C. Jiang, Y. T. Lee, S. H. Lin, and C. K. Ni, Aust. J. Chem. **54**, 561 (2001).
[14] C. K. Lin, C. L. Huang, J. C. Jiang, H. Chang, S. H. Lin, Y. T. Lee, and C. K. Ni, J. Am. Chem. Soc. **124**, 4068 (2002).
[15] C. L. Huang, J. C. Jiang, S. H. Lin, Y. T. Lee, and C. K. Ni, J. Chem. Phys. **116**, 7779 (2002).
[16] C. L. Huang, J. C. Jiang, Y. T. Lee, and C. K. Ni, J. Chem. Phys. **117**, 7034 (2002).
[17] C. L. Huang, J. C. Jiang, Y. T. Lee, and C. K. Ni, J. Phys. Chem. A **107**, 4019 (2003).
[18] M. F. Lin, C. L. Huang, Y. T. Lee, and C. K. Ni, J. Chem. Phys. **119**, 2032 (2003).
[19] C. L. Huang, J. C. Jiang, A. Mebel, Y. T. Lee, and C. K. Ni, J. Am. Chem. Soc. **125**, 9814 (2003).
[20] M. F. Lin, C. L. Huang, Y. T. Lee, and C. K. Ni, J. Chem. Phys. **119**, 7701 (2003).
[21] T. Shibata and T. Suzuki, Chem. Phys. Lett. **262**, 115 (1996).
[22] J. K. Foote, M. H. Mallon, and J. N. Pitts Jr, J. Am. Chem. Soc. **88**, 3698 (1966).
[23] K. Shindo, and S. Lipsky, J. Chem. Phys. **45**, 2292 (1966).
[24] H. R. Ward and J. S. Wishnok, J. Am. Chem. Soc. **90**, 5353 (1968).
[25] N. Nakashima and K. Yoshihara, J. Chem. Phys. **79**, 2727 (1983).
[26] P. Reilly and K. L. Kompa, J. Chem. Phys. **73**, 5468 (1980).
[27] W. Radloff, T. Freudenberg, H. H. Ritze, V. Stert, F. Noack, and I. V. Hertel, Chem. Phys. Lett. **261**, 301 (1996).
[28] H. R. Ward, J. S. Wishnok, and P. D. Sherman Jr, J. Am. Chem. Soc. **89**, 162 (1967).
[29] L. Kaplan and K. E. Wilzbach, J. Am. Chem. Soc. **89**, 1030 (1967).

[30] L. Kaplan, S. P. Walch, and K. E. Wilzbach, J. Am. Chem. Soc. **90**, 5646 (1968).
[31] F. Mellows and S. Lipsky, J. Phys. Chem. **70**, 4076 (1966).
[32] D. Bryce-Smith and A. Gilber, Tetrahedron **32**, 1309 (1976).
[33] K. E. Wilzbach, J. S. Ritcher, and L. Kaplan, J. Am. Chem. Soc. **89**, 1031 (1968).
[34] A. Yokoyama, X. Zhao, E. J. Hintsa, R. E. Continetti, and Y. T. Lee, J. Chem. Phys. **92**, 4222 (1990).
[35] M. Mebel, S. H. Lin, X. M. Yang, and Y. T. Lee, J. Phys. Chem. **101**, 6781 (1997).
[36] A. M. Mebel, M. C. Lin, D. Chakraborty, J. Park, S. H. Lin, and Y. T. Lee, J. Chem. Phys. **114**, 8421 (2001).
[37] M. Dzvonik, S. Yang, and R. Bersohn, J. Chem. Phys. **61**, 4408 (1974).
[38] A. Freedom, S. C. Yang, M. Kawasaki, and R. Bersohn, J. Chem. Phys. **72**, 1028 (1980).
[39] H. Zhang, R. S. Zhu, G. J. Wang, K. L. Han, G. Z. He, and N. Q. Lou, J. Chem. Phys. **110**, 2922 (1999).
[40] K. L. Han, G. Z. He, and N. Q. Lou, Chem. Phys. Lett. **203**, 509 (1993).
[41] G. J. Wang, R. S. Zhu, H. Zhang, K. L. Han, G. Z. He, and N. Q. Lou, Chem. Phys. Lett. **288**, 429 (1998).
[42] T. Ichimura, Y. Mori, H. Shinohara, and N. Nishi, Chem. Phys. **189**, 117 (1994).
[43] T. Ichimura, Y. Mori, H. Shinohara, and N. Nishi, Chem. Phys. Lett. **122**, 51 (1985).
[44] M. Kawasaki, K. Kasatani, H. Sato, H. Shinohara, and N. Nishi, Chem. Phys. **88**, 135 (1984).
[45] T. Ichimura, Y. Mori, H. Shinohara, and N. Nishi, J. Chem. Phys. **107**, 835 (1997).
[46] S. Satyapal, S. Tasaki, and R. Bersohn, Chem. Phys. Lett. **203**, 349 (1993).
[47] R. S. Zhu, H. Zhang, G. J. Wang, X. Gu, K. L. Han, G. Z. He, and N. Q. Lou, Chem. Phys. **248**, 285 (1999).
[48] T. Ichimura, A. Shimoda, T. Kikuchi, Y. Kohso, T. Hikid, and Y. Mori, J. Photochem. **31**, 157 (1985).
[49] I. Howe and D. H. Williams, J. Am. Chem. Soc. **91**, 7137 (1969).
[50] T. Nishimura, G. Meisels, and Y. Niwa, Bull. Chem. Soc. Jpn **64**, 2894 (1991).
[51] K. E. Wilzbach and L. Kaplan, J. Am. Chem. Soc. **86**, 2307 (1964).
[52] A. W. Burgstahler and P. L. Chien, J. Am. Chem. Soc. **86**, 2940 (1964).
[53] L. Kaplan, K. E. Wilzbach, W. G. Brown, and S. S. Yang, J. Am. Chem. Soc. **87**, 675 (1965).
[54] K. E. Wilzbach and L. Kaplan, J. Am. Chem. Soc. **87**, 4004 (1965).
[55] I. E. Den Besten, L. Kaplan, and K. E. Wilzbach, J. Am. Chem. Soc. **90**, 5868 (1968).
[56] D. Bryce-Smith and A. Gilbert, in *Rearrangement in Ground and Excited States*, Vol. 3, edited by P. De Mayo (Academic Press, New York, 1980).
[57] A. H. Jackson, G. W. Kenner, G. McGillvray, and G. S. Sach, J. Am. Chem. Soc. **87**, 675 (1965).
[58] K. E. Wilzbach, A. L. Harkness, and L. Kaplan, J. Am. Chem. Soc. **90**, 1116 (1968).
[59] J. Park, R. Bersohn, and I. Oref, J. Chem. Phys. **93**, 5700 (1990).
[60] Y. Kajii, K. Obi, I. Tanaka, N. Ikeda, N. Nakashima, and K. Yoshihara, J. Chem. Phys. **86**, 6115 (1987).
[61] N. Ikeda, N. Nakashima, and K. Yoshihara, J. Chem. Phys. **82**, 5285 (1985).
[62] H. Hippler, V. Schubert, J. Troe, and H. Wendelken, J. Chem. Phys. Lett. **84**, 253 (1981).
[63] J. Troe and W. Wieters, J. Chem. Phys. **71**, 3931 (1979).
[64] R. Srinivasan, J. Am. Chem. Soc. **84**, 3432 (1962).
[65] B. A. Thrush and J. J. Zwolenik, Bull. Soc. Chim. Belg. **71**, 642 (1962).
[66] N. Nakashima and K. Yoshihara, J. Phys. Chem. **93**, 7763 (1989).
[67] K. Tsukiyama and R. Bersohn, J. Chem. Phys. **86**, 745 (1987).
[68] U. Brand, H. Hippler, L. Lindemann, and J. Troe, J. Phys. Chem. **94**, 6305 (1990).
[69] K. Luther, J. Troe, and K. L. Weitzel, J. Phys. Chem. **94**, 6316 (1990).
[70] S. Lange, K. Luther, T. Rech, A. M. Schmoltner, and J. Troe, J. Phys. Chem. **98**, 6509 (1994).
[71] T. Shimada, Y. Ojima, N. Nakashima, Y. Izawa, and C. Yamanaka, J. Phys. Chem. **96**, 6298 (1992).
[72] R. Fröchtenicht, J. Chem. Phys. **102**, 4850 (1994).

[73] D. R. Borst and D. W. Pratt, J. Chem. Phys. **113**, 3658 (2000); D. R. Borst, P. W. Joireman, D. W. Pratt, E. G. Robertson, and J. P. Simons, J. Chem. Phys. **116**, 7057 (2002).
[74] T. G. Dietz, M. A. Duncan, M. G. Liverman, and R. E. Smalley, J. Chem. Phys. **76**, 1227 (1982).
[75] H. Lohmannsroben, G. K. Luther, and M. Stuke, J. Phys. Chem. **91**, 3499 (1987).